


Enhanced activity of Alzheimer disease associated variant of protein kinase C drives cognitive decline in a mouse model

Received: 10 September 2021

Accepted: 1 November 2022

Published online: 23 November 2022

 Check for updates


Gema Lordén¹, Jacob M. Wozniak^{1,2}, Kim Doré³, Lara E. Dozier⁴, Chelsea Cates-Gatto⁵, Gentry N. Patrick⁴, David J. Gonzalez^{1,2}, Amanda J. Roberts⁵, Rudolph E. Tanzi⁶ ⁶ Alexandra C. Newton ¹ 

Exquisitely tuned activity of protein kinase C (PKC) isozymes is essential to maintaining cellular homeostasis. Whereas loss-of-function mutations are generally associated with cancer, gain-of-function variants in one isozyme, PKC α , are associated with Alzheimer's disease (AD). Here we show that the enhanced activity of one variant, PKC α M489V, is sufficient to rewire the brain phosphoproteome, drive synaptic degeneration, and impair cognition in a mouse model. This variant causes a modest 30% increase in catalytic activity without altering on/off activation dynamics or stability, underscoring that enhanced catalytic activity is sufficient to drive the biochemical, cellular, and ultimately cognitive effects observed. Analysis of hippocampal neurons from PKC α M489V mice reveals enhanced amyloid- β -induced synaptic depression and reduced spine density compared to wild-type mice. Behavioral studies reveal that this mutation alone is sufficient to impair cognition, and, when coupled to a mouse model of AD, further accelerates cognitive decline. The druggability of protein kinases positions PKC α as a promising therapeutic target in AD.

Alzheimer's disease (AD), the most common neurodegenerative disorder in elderly individuals, is characterized by degeneration of synapses, neuronal death, and ultimately, a reduction in the size of brain regions involved in learning and memory¹. In addition, AD brains are distinguished by the presence of neurofibrillary tangles and extracellular amyloid- β (A β) plaques, which lead to cognitive impairment^{2–4}. However, the molecular mechanisms underlying AD remain elusive. Currently, one of the strongest hypotheses linked to AD development is the abnormal accumulation of the A β 42 peptides, produced by the improper processing of the amyloid precursor protein (APP) by β - and γ -secretases^{5,6}. Specifically, soluble A β oligomers

are considered to be the neurotoxic species that initiate the disease and its accompanying symptoms. The A β plaques, however, are comparatively inert, but may function as reservoirs of the diffusible oligomers⁷. APP and presenilin genes (*PSEN* and *PSEN2*) were among the first genes shown to have variants associated with AD and were crucial to developing the amyloid cascade hypothesis and establishing the association between misprocessing and deposition of A β plaques and AD development^{8–11}. Although these variants account for a relatively low percentage of the cases of AD, their identification paved the way to explore the complex genetics associated with the disease¹². Polymorphisms in *APOE* were also established early on as being a

¹Department of Pharmacology, University of California San Diego, La Jolla, CA 92093, USA. ²Skaggs School of Pharmacy and Pharmaceutical Sciences, University of California San Diego, La Jolla, CA 92093, USA. ³Center for Neural Circuits and Behavior, Department of Neurosciences, University of California San Diego, La Jolla, CA 92093, USA. ⁴Section of Neurobiology, Division of Biological Sciences, University of California San Diego, La Jolla, CA 92093, USA. ⁵Animal Models Core Facility, The Scripps Research Institute, La Jolla, CA 92037, USA. ⁶Genetics and Aging Research Unit, McCance Center for Brain Health, Department of Neurology, Massachusetts General Hospital and Harvard Medical School, Charlestown, MA 02129, USA.

 e-mail: anewton@health.ucsd.edu

strong risk factor for AD^{13–15}. Whole-genome sequencing efforts are identifying other genetic variants associated with AD risk, including polymorphisms in genes such as *TREM2*, *PLCG2*, and *AB13* among others^{16–20}. In a recent search for rare functional variants associated with AD, analysis of whole-genome sequencing data from 410 families of affected and unaffected siblings from the NIMH cohort identified variants in PKC α . One of these variants, M489V (rs34406842, minor allele frequency of 0.00095 in gnomad), was present only in affected members and no unaffected members of 4 families, cosegregating with AD affection status²¹. The high druggability of protein kinases poises PKC α as a potential target in AD therapies.

PKC α belongs to the Ca²⁺- and diacylglycerol (DG)-dependent class of PKC isozymes referred to as conventional PKC. These Ser/Thr kinases transduce signals from receptor-mediated hydrolysis of membrane phospholipids, which generates their activators, Ca²⁺ and DG^{22–24}. Conventional PKC isozymes play critical roles in maintaining cellular homeostasis, where their finely tuned activity regulates the balance between cell death and survival. They are primed by a series of ordered phosphorylations required for them to adopt a stable, auto-inhibited conformation poised to respond to second messengers rapidly and reversibly. Aberrant PKC that is not properly autoinhibited is shunted to degradation by quality control pathways²⁵. Although PKC has historically been assumed to be oncogenic, recent analysis has reframed PKC isozymes as having tumor-suppressive roles. Notably, cancer-associated mutations are generally loss-of-function, and elevated protein levels of PKC isozymes confer improved survival for many cancers^{26,27}. For this reason, inhibition of PKC in cancer has been unsuccessful, and, in some cases, worsened patient outcome²⁸. The identification of activity-enhancing variants of PKC α that co-segregate with AD²¹ opens the possibility that this disease could benefit from repurposing PKC inhibitors originally used in cancer clinical trials.

In marked contrast to cancer, gain-of-function mutations in PKC α have been shown to co-segregate with AD²¹. The identification of highly penetrant germline variants in PKC α in families with LOAD highlighted deregulated PKC function as potentially causative in AD²¹. Consistent with the involvement of PKC in the pathology of AD, unbiased phosphoproteomics studies have identified augmented phosphorylation of PKC substrates, including myristoylated alanine-rich C-kinase substrate (MARCKS), as one of the main events in AD development^{29,30}. Additionally, electrophysiological studies have established that PKC α is necessary for A β -dependent synaptic depression, by a mechanism that requires the PDZ ligand of this PKC isozyme^{21,31}. This PDZ ligand targets PKC α to the scaffolds PSD95, SAP97, and PICK1, with this latter scaffold also being necessary for A β -dependent synaptic depression^{31–33}. All AD-associated variants in PKC α described to date are gain-of-function^{21,34}. Biochemical analysis of one variant present in four unrelated families, M489V PKC α , reveals that the Met to Val substitution in the activation loop increases the intrinsic catalytic rate of the enzyme by ~30% without affecting stabilizing autoinhibitory constraints, and consequently, evades the cell's homeostatic degradation of aberrantly active PKC α ³⁴. Taken together, these results support a model in which the activity of PKC α at post-synaptic scaffolds mediates the effects of A β , with enhanced activity contributing to the pathology of AD. Determining whether AD-associated mutations in PKC α are sufficient to drive the pathology of AD would inform on whether PKC α inhibition is a potential therapeutic strategy in AD.

In the present study, we used genome editing to introduce the M489V gain-of-function variant into endogenous PKC α in order to determine whether this single amino acid change, modestly enhancing kinase activity, is sufficient to drive the pathology of AD in a mouse model. Biochemical, phosphoproteomic, electrophysiological, and behavioral studies revealed that elevated PKC activity conferred by the presence of this AD variant leads to increased phosphorylation of PKC substrates in the brain, neurite degeneration, enhanced A β driven synaptic depression, and cognitive decline, which is more evident and

more rapid on the background of a transgenic mouse model of AD. These data establish that enhanced PKC α activity is sufficient to drive cognitive decline in a mouse model and support inhibition of PKC α as a potential therapeutic approach in AD.

Results

Altered brain phosphoproteome in M489V PKC α mice

PKC α M489V is an AD-associated mutation that has been shown to be more catalytically active than wild-type (WT) PKC α by a mechanism that does not compromise its stability, allowing it to evade the cell's homeostatic down-regulation of aberrantly active PKC α ³⁴. To identify phosphorylation events that occur in the brain as a result of increased PKC α activity, brains from C57BL/6 mice harboring WT and the M489V mutation in PKC α were isolated at 3 months of age and subjected to phosphoproteomic analysis. Briefly, proteins were extracted and digested from brain lysates and phosphopeptides were enriched with TiO₂. Unenriched peptides and phosphopeptides were labeled with TMT 10-plex reagents, and analyzed by liquid chromatography-MS2/MS3 (LC-MS3) to quantify the proteome and phosphoproteome (Fig. 1a). We quantified 10,208 phosphopeptides per sample representing 1899 proteins with a false discovery rate (FDR) of <1% at peptide and protein level (Dataset S1). The median within sample coefficient of variation was ~20% on average, indicating minimal variance (Supp Fig. 1b). The phosphosite distribution was 80.98 phosphoserine (pS), 17.00 phosphothreonine (pT), and 2.02 phosphotyrosine (pY), with most of the peptides phosphorylated on single (68.32%) and double (26.33%) sites and fewer on triple (4.64%) and quadruple (0.71%) sites (Supp Fig. 1c, d).

The presence of the M489V PKC α variant induced significant changes in a variety of phosphoproteins (Fig. 1b and Supp Fig. 1f). Specifically, M489V PKC α induced significant changes in a total of 829 phosphopeptides. Of those, 430 peptides from 270 unique proteins had increased phosphorylation (red) and 399 peptides from 261 unique proteins had decreased phosphorylation (blue) (Fig. 1b; Supp Table 1 presents the top 25 peptides whose phosphorylation increased in PKC α M489V brain). Among the peptides with increased phosphorylation in the brains of mice harboring the M489V variant of PKC α , we found increased phosphorylation of Ser156 and Ser163 from MARCKS, a *bona fide* PKC substrate (Fig. 1b, c). Increased phosphorylation of MARCKS, in particular, is consistent with the previously reported increased catalytic activity of purified PKC α M489V compared to WT³⁴, an increase also observed for PKC α immunoprecipitated from brain lysates of the M489V mice (Supp Fig. 1g). Importantly, immunoblot analysis of brain lysates from littermates of the mice used for mass spectrometry analysis has previously established that the amount of PKC α protein did not change in brains from WT and M489V mice³⁴ (see also Supp Fig. 1h), consistent with our biochemical studies which demonstrated that the M489V mutation in PKC α does not alter the steady-state levels of the protein³⁴.

Next, we evaluated the changes in the phosphoproteome caused by the presence of PKC α M489V in heterozygosity or in homozygosity using k-means clustering of the phosphopeptides whose phosphorylation changed significantly among the three groups (Supp Fig. 1e). The PKC α M489V-induced phosphoproteome separated into four different clusters, with cluster 2 (C2) and cluster 3 (C3) displaying the peptides whose phosphorylation decreased or increased, respectively, in a gene-dosage dependent manner (Fig. 1d, e, Supp Fig. 1e). To explore the biological functions associated with the enhanced kinase activity derived from the AD variant in PKC α , we used gene ontology (GO) enrichment analysis to compare the cellular compartments represented in C2 (phosphorylation of substrates decreased in a gene-dosage dependent manner) and C3 (phosphorylation increased in a gene-dosage dependent manner) (Fig. 1d, e). Post-synaptic density, synapse, cell junction, and post-synaptic membrane were significantly enriched in the group of peptides whose phosphorylation decreased in

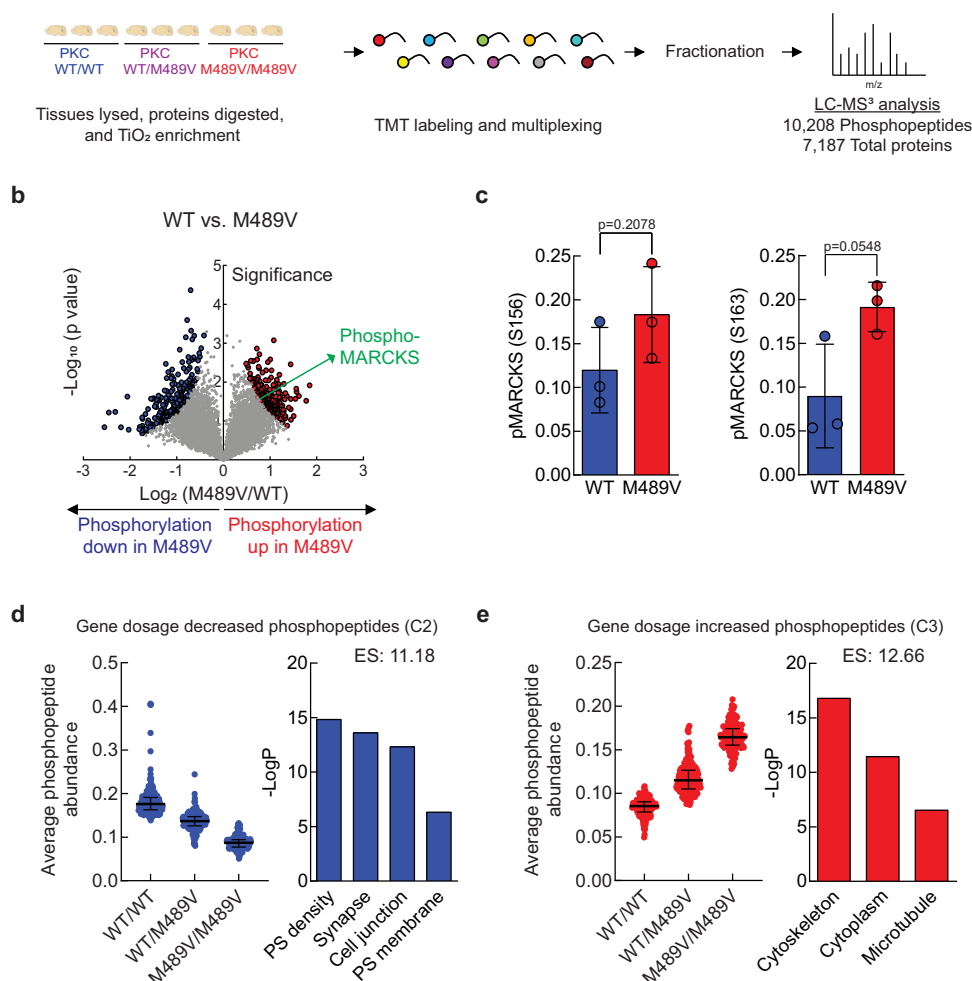


Fig. 1 | Phosphoproteomics analysis of brains from 3-month-old WT mice and mice harboring the PKC M489V mutation on C57BL/6 background.

a Experimental design. Brains from WT (blue), heterozygous (purple), or homozygous (red) mice were subjected to phosphoproteomics analysis. 7187 proteins and 10,208 phosphopeptides were quantified per sample in the standard proteomics and phosphoproteomics analyses, respectively. **b** Volcano plot of phosphopeptides quantified from brains from WT mice and M489V homozygous mice. The \log_{10} -transformed p values associated with individual phosphopeptides are plotted against the \log_2 -transformed fold change in abundance between WT and M489V homozygous brains. Color intensities depict peptides whose phosphorylation level is significantly higher (red) or lower (blue) in M489V homozygous mice compared to WT. Significance was determined at a p score cutoff of < 0.05 , and p values for calculating p scores were generated with a two-tailed Student's t test not corrected for multiple hypotheses. **c** Graph showing the quantification of two

MARCKS phosphopeptides in brains from WT (blue) and M489V homozygous (red) mice indicates the mean \pm SD (p values determined using a two-tailed Student's t test). **d** Left: graph showing the distribution of peptides whose phosphorylation significantly decreased (values of $p < 0.05$ using a two-tailed Student's t test) in a gene-dose dependent manner (WT > WT/M489V > M489V/M489V). Graph depicts the median \pm interquartile range. Right: GO enrichment analysis from these peptides using DAVID. (ES = enrichment score, PS = post-synaptic). **e** Left: graph showing the distribution of peptides whose phosphorylation significantly increased (values of $p < 0.05$ using a two-tailed Student's t test) in a gene-dose dependent manner (WT < WT/M489V < M489V/M489V). Graph depicts the median \pm interquartile range. Right: GO enrichment analysis from these peptides using DAVID. Data in **b–e** are representative from $n = 3$ biological independent samples for each genotype. Source data for **c–e** are provided in the Source Data file.

a gene-dosage-dependent manner (C2) (Fig. 1d, right). However, peptides whose phosphorylation increased as a function of the variant (C3) showed significant enrichment in cytoskeleton, cytoplasm, and microtubule function (Fig. 1e, right). These data are consistent with enhanced PKC α function increasing the phosphorylation of direct substrates such as MARCKS to modulate cytoskeletal function, and indirectly decreasing the phosphorylation of substrates that are key regulators of the synapse, either by enhancing phosphatase activity or inhibiting kinases directed at these substrates.

Spine density loss in hippocampal neurons of M489V PKC mice

Given that post-synaptic proteins were one of the most altered in the phosphoproteomic analysis of M489V brain, we examined whether the synapses in the M489V mice had an altered morphology compared to those from WT mice. The post-synaptic component of excitatory

synapses in the brain is comprised of small extensions on dendrites known as dendritic spines^{35,36}. The morphology of the spines is an indicator of the stability, plasticity, and strength of associated synapses. The majority of excitatory synapses in the brain exist on dendritic spines and, accordingly, the regulation of dendritic spine density in the hippocampus is considered to play a central role in learning and memory^{37,38}. To better understand the link between enhanced PKC activity and neurodegeneration, we examined spine density in hippocampal neurons from 4.5-month-old littermate male WT mice or mice homozygous for the PKC α M489V variant. We observed a slight (9.81 ± 0.02), but statistically significant, reduction in the number of spines per micron in the M489V homozygous mice compared with littermate WT mice, as assessed by fluorescence staining of neuronal projections (Fig. 2a, b). Furthermore, western blot analysis of isolated hippocampi revealed a general increase in the phosphorylation of PKC substrates in the PKC α

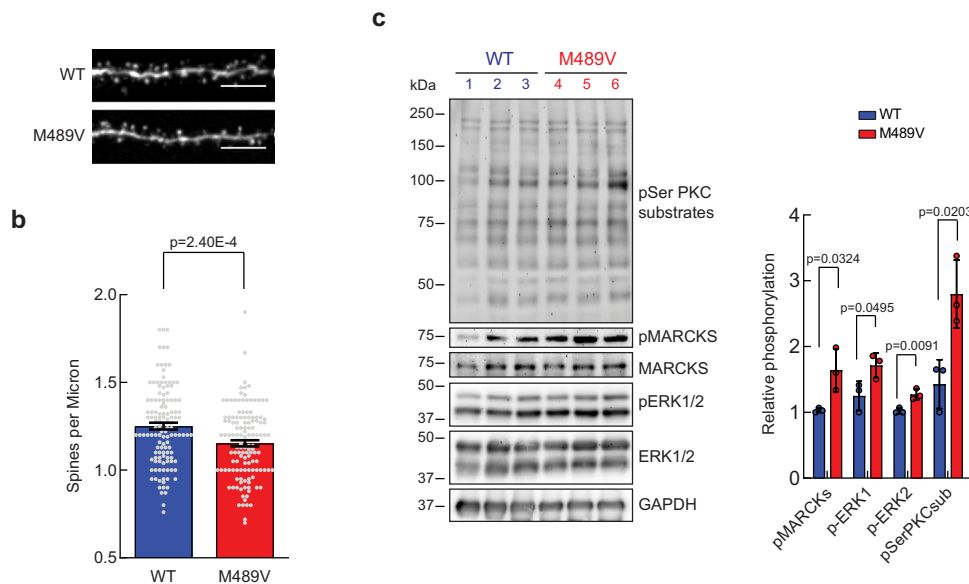


Fig. 2 | The AD-associated PKC M489V mutation reduces spine density and increases PKC substrate phosphorylation in the hippocampus. **a** Representative immunofluorescence image of dendritic segments from hippocampal neurons injected with Alexa Fluor® 594 Hydrazide to follow neuronal projections (dendritic segment = 20 μ m in length, scale bar 5 μ m). $n = 129$ dendritic segments from 6 mice of each genotype were analyzed. **b** Average number of spines per micron in neurons isolated from 4–5-month-old WT or littermates M489V PKC α homozygous male mice ($n = 6$ mice of each genotype). Spines were counted in separate spine segments (10–25 μ m in length). Data show a spine density reduction of $\sim 10\%$, from 1.25 ± 0.02 spines/ μ m to 1.15 ± 0.02 spines/ μ m in the M489V mice. $n = 129$ dendritic segments (over 1500 spines) were analyzed. Error bars show standard error of the mean. ($p = 2.40E-4$ using unpaired two-tailed Student's t test). **c** Left. Immunoblots

of lysates of hippocampi obtained from WT mice (lanes 1–3, blue) or M489V mice (lanes 4–6, red). Right. Relative phosphorylation represents the densitometric analyses of the western blot phosphorylation signal and the total antibody signal of the indicated substrates. pERK1/2 (T202/Y204 for ERK1 and T185/Y187 for ERK2) and pMARCKS (S159/S163) signal was normalized to total ERK1/2 and total MARCKS signal respectively, and phospho-Ser PKC substrates signal was normalized to its GAPDH loading control. Data were normalized to the WT1 values, and normalized data from the depicted western blots were plotted as average normalized intensity \pm SEM (p values were determined using a two-tailed Student's t test). Data are representative of $n = 3$ biologically independent experiments. Source data and uncropped blots are provided in the Source Data file.

M489V samples compared to WT (Fig. 2c). The phosphorylation of MARCKS at Ser159/Ser163 (Fig. 2c) was also increased in the PKC α M489V hippocampal samples, consistent with the whole brain phosphoproteomics data (Figs. 1b, c) and previously validated by western blot³⁴. Additionally, the phosphorylation of the extracellular signal-regulated kinase (ERK) 1/2, a MAP kinase family member, was enhanced in the PKC α M489V hippocampi compared to those from WT mice (Fig. 2c). In summary, the PKC α M489V variant mice display reduced spine density, as well as enhanced phosphorylation of proteins that regulate neurites, an important hallmark of Alzheimer's disease.

Impaired cognition of PKC M489V mice on a C57BL/6 background

Because loss-of-spine density in the hippocampus correlates with decreased learning ability³⁹, we next assessed whether the PKC α M489V variant impacted cognition. We examined the behavior of WT and M489V mice on the Barnes maze, a test that has been widely used to assess spatial learning and memory in AD⁴⁰. In this test, mice are trained to use distinct cues around the maze to find an escape box under one of 20 holes around the perimeter of a round platform (Fig. 3a). After the training period, the escape tunnel is removed, and the amount of time that mice spend in each quadrant (the target quadrant vs non-target quadrants) searching for the hole is recorded. Cognitively intact mice spend more time in the target quadrant relative to the other areas of the maze, whereas mice with impaired cognition do not discriminate well between the four quadrants. WT mice of all ages performed well on this test, spending approximately twice as long in the target quadrant compared to the other quadrants (Fig. 3b–d). In marked contrast, mice harboring the M489V mutation spent progressively less time in the target quadrant with age, such that at 12 months, they no longer discriminated between the target and

other quadrants (Fig. 3d). Even at 3 months of age, their ability to recognize the target quadrant was decreased relative to the WT mice (34 ± 2 vs 41 ± 5 of time in target quadrant, respectively). This reduced time in the target quadrant was not a reflection of impaired locomotion, as activity levels were the same in WT and M489V mice in both the Barnes maze probe test and an independent test of activity (Supp Fig. 2a and Supp Fig. 2b). Additionally, the M489V mice did not show increased anxiety as assessed by the light/dark test (Supp Fig. 2c). Thus, the M489V mice had impaired learning and memory but not alterations in mobility or anxiety compared with the WT mice. These results establish that the AD-associated mutation M489V in PKC α is sufficient to cause cognitive decline in C57BL/6 mice.

Enhanced A β induced synaptic depression in neurons of PKC M489V mice

Alzheimer's disease is characterized by the presence of neuritic plaques, which primarily consist of A β peptides derived from APP proteolysis^{41,42}. These A β aggregates are known to degrade synapses and impair memory formation^{31,43}. Because PKC α is necessary for A β -induced synaptic depression^{21,31,44}, we reasoned that the enhanced activity of the PKC α M489V AD mutation might enhance electrophysiological responses to A β . Organotypic hippocampal slices from WT or M489V mice were infected with a Sindbis viral vector that expresses CT100, a product of APP cleavage by β -secretase. As a result of CT100 expression, A β peptide production increases in infected neurons due to processing by β -secretase^{6,45,46}, resulting in synaptic depression^{45,47–49}. Synaptic transmission was studied 18–24 h after infection by obtaining whole-cell recordings from two neighboring pyramidal hippocampal CA1 neurons, one infected and one uninfected; electric stimulation of Shaffer collateral axons was used to elicit AMPAR-mediated excitatory post-synaptic currents (EPSCs) (Fig. 4a).

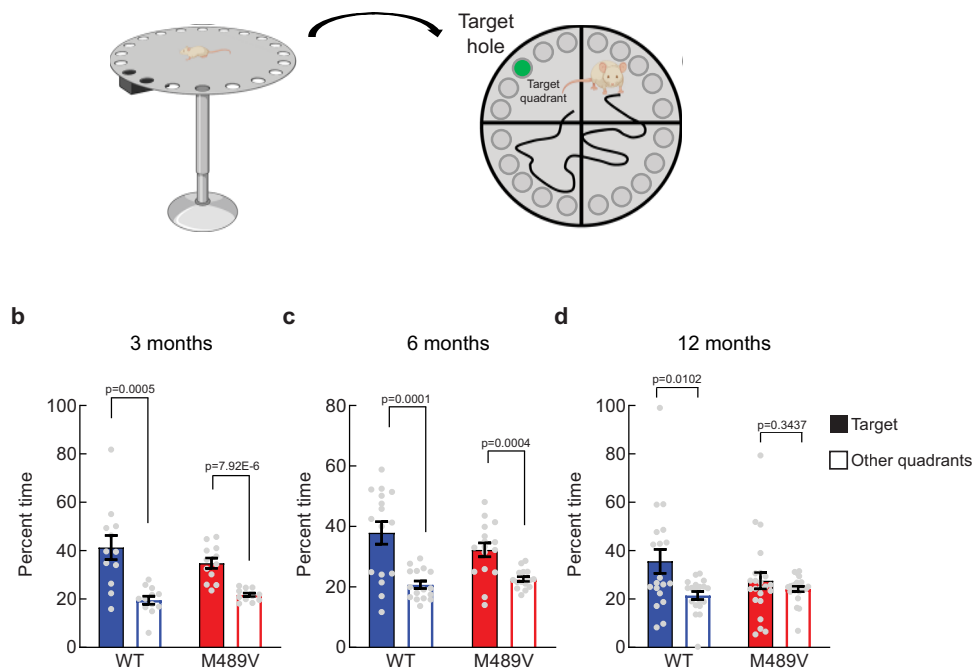


Fig. 3 | Impaired spatial learning and memory in C57BL/6 PKC M489V/M489V mice in the Barnes maze test. **a** Schematic of the Barnes maze test. Created with Biorender.com. **b–d** Percent time spent in the target quadrant (filled bars) versus the average of the other quadrants (open bars) in the probe test in separate groups of 3 (**b**), 6 (**c**), and 12 (**d**) months old mice. Group sizes: 3-month (WT: 4 males, 8 females, M489V littermates: 6 males, 6 females), 6-month (WT: 8 males, 8 females, M489V littermates: 8 males, 8 females), 12 month (WT: 7 males, 12 females, M489V littermates: 12 males, 11 females). Error bars show standard error of the mean. No statistically significant sex differences were found. ANOVA was used for statistical analysis, followed by post hoc two-tailed Student's *t* test to determine the *p* values. Source data are provided in the Source Data file.

Such cell-pair recordings permit one to compare directly the impact of elevated A β on synaptic transmission, as the number of activated Shaffer collateral axons targeting infected and non-infected cells is on average the same, irrespective of the stimulation intensity. As expected^{48,49}, neurons expressing CT100 displayed synaptic depression compared to uninfected neighboring neurons in both WT and M489V slices. However, this effect was more pronounced in the slices from the M489V mice (26 \pm 12% depression in WT mice; 55 \pm 6% depression in M489V mice; $p < 0.05$; Fig. 4b–d). These results indicate that A β -dependent synaptic depression in neurons is enhanced by the presence of a more active PKC α , supporting a model in which increased PKC activity drives the synaptic loss associated with AD.

Phosphoproteomic profiling of tg-AD mouse with M489V PKC variant

The enhanced synaptic depression induced by A β in PKC α M489V hippocampal neurons compared to WT neurons led us to next address whether the pathology associated with the gain-of-function PKC α mutation aggravates the effects caused by the presence of the APP. To this end, the M489V mutation was introduced onto a B6;SJL mouse with the APP transgene carrying the Swedish mutation (tg-AD); this well-established mouse model has a predisposition to AD as a result of elevated A β levels caused by abnormal processing of the mutant APP by β -secretase⁵⁰. We first investigated whether the introduction of the PKC α M489V mutation into the tg-AD mouse model with the APP_{sw} transgene impacted the presence of soluble and insoluble A β in the brain. Brains were homogenized and different fractions of A β were extracted and analyzed by enzyme-linked immunosorbent assay (ELISA). The levels of A β 40 and A β 42, as well as the A β 42/A β 40 ratio, were the same in mice with WT PKC α or the M489V variant (Supp Fig. 3a–c). These results were confirmed by histochemical analyses, where brains both WT tg-AD and M489V tg-AD mice presented similar levels of A β plaques (Supp Fig. 3d). This suggests that the molecular events by which enhanced

PKC α activity leads to neurodegeneration and cognitive decline are downstream or independent of A β -production.

Given that the PKC α M489V variant did not influence A β -production in the tg-AD mouse model, we reasoned it is signaling downstream of A β and could further deregulate the phosphoproteome, on top of the changes induced by the APP_{sw} transgene. We thus examined whether the PKC α M489V altered the phosphoproteome in the AD mouse model in a similar fashion as the alterations observed on the non tg-AD background. Brains from mice harboring WT or M489V PKC α in the presence (WT tg-AD/M489V tg-AD) or absence (WT non tg-AD/M489V non tg-AD) of the APP_{sw} transgene were isolated at 4.5 and 6 months of age. Tissues were processed and analyzed as in Fig. 1a to quantify the proteome and phosphoproteome (Fig. 5a). We quantified ~12,000 phosphopeptides per sample, representing ~6500 proteins with an FDR of <1% at the peptide and protein level (Dataset S2). The median within sample coefficient of variation was, on average, <20%, indicating minimal variance (Supp Fig. 4a). Consistent with previous experiments, the phosphosite distribution was 77.41% phosphoserine (pS), 19.40% phosphothreonine (pT), and 3.19% phosphotyrosine (pY) (Supp Fig. 4b), with most of the peptides phosphorylated on single (73.60%) and double (23.10%) sites, and fewer on triple (2.96%) and quadruple (0.35%) sites (Supp Fig. 4c).

We next analyzed the APP and PKC α levels in the different cohorts of mice. As expected, the amount of APP was consistently elevated in all the tg-AD mice (WT tg-AD/M489V tg-AD). Notably, the relative abundance of PKC α was the same for every group (Fig. 5b). These data highlight the reproducibility of this analysis and validate our biochemical studies³⁴ showing that the M489V mutation does not alter the stability/steady-state levels of PKC α in vivo. Western blot analysis of whole brain lysate revealed that the APP transgene increased PKC activity, as observed by increased phosphorylation of PKC substrates in the brains of mice carrying the APP transgene compared with the control mice (Fig. 5c). This is consistent with the phosphoproteomic

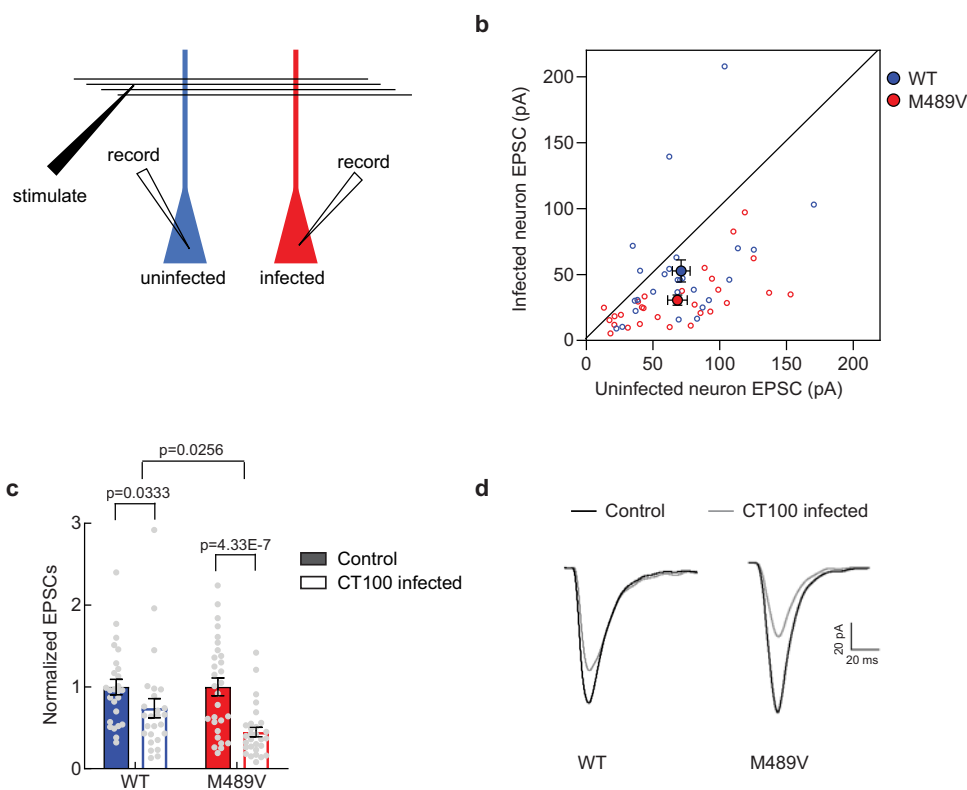


Fig. 4 | The AD-associated PKC M489V mutation exacerbates A β -induced synaptic depression. **a** Experimental design of dual-patch whole-cell recordings (see Material and Methods section). **b** Dot plot showing the individual excitatory post-synaptic currents (EPSCs) in CT100 infected versus uninfected CA1 hippocampal neurons from WT (blue open circles, $N = 26$) and M489V (red open circles, $N = 29$) mice. Group averages indicated by filled circles, error bars indicate SEM. **c** Bar graph of dual-patch recordings for indicated groups (same data as in **b**, $n = 26$ wt and $n = 29$ M489V CA1 hippocampal neurons); responses were normalized to

uninfected controls (solid bars) and graph depicts the mean \pm SEM. Paired two-tailed t tests were used to assess statistical significance of dual-patch recordings and obtain p values. To compare CT100-induced depression in WT versus M489V mice, two-way ANOVA was performed ($p < 0.0001$), followed with Newman-Keuls multiple comparison post hoc test to determine the p value. **d** Representative traces (mean of at least 40 consecutive trials) obtained from evoked AMPA-receptor-mediated responses from WT and M489V CA1 hippocampal neurons. Source data are provided in the Source Data file.

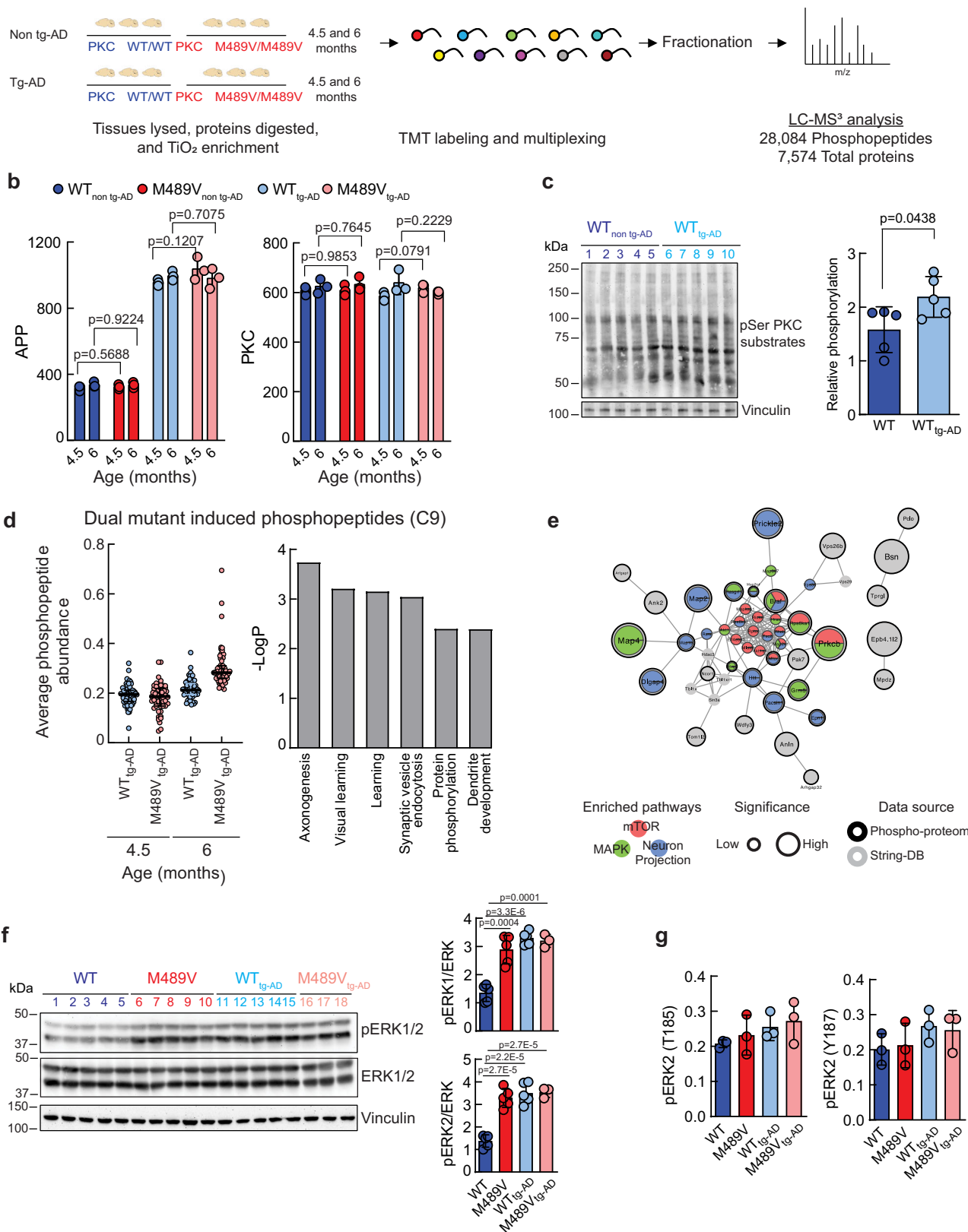
analysis which revealed increases in a large number of substrates (top 25 phosphosites enhanced by PKC-M489V in the tg-AD mice are presented in Supp. Tables 2 and 3).

Analysis of the changes in the phosphoproteome resulting from the introduction of the PKC α M489V mutation in an AD mouse model, using k -means clustering of the 28,084 phosphopeptides, revealed nine distinct clusters (Supp Fig. 4d). The age-related phosphoproteome clustered into three distinct groups: C1, C6, and C8. C1 and C8 contained peptides whose phosphorylation increased with age, while C6 contained peptides that displayed a modest decrease in phosphorylation with age. M489V caused an increase in phosphorylation only at the early age group (4.5 months) in the C2 and C4 clusters of the APP brain phosphoproteome. The C3 and C5 clusters contained peptides whose phosphorylation decreased at 4.5 months. C9 was of particular interest (Supp Fig. 4d) as it contained proteins whose phosphorylation increased only slightly from 4.5 months to 6 months of age in tg-AD mice with WT PKC α , but increased substantially with age in mice harboring the PKC α M489V variant (Fig. 5d, left). We reasoned that this set comprised proteins whose phosphorylation increased with age in the tg-AD background in a manner that was exacerbated with the PKC α mutation. To explore the biological functions associated with this distinct phosphoproteome, we analyzed the biological processes that were overrepresented in C9 using GO analysis. Learning, axonogenesis, and synaptic vesicle endocytosis were significantly enriched in C9, as well as protein phosphorylation, and dendrite development (Fig. 5d, right). In addition, String analysis revealed that many of these proteins were part of the mTOR signaling

pathway, the mitogen-activated protein kinase (MAPK) signaling pathway and involved in neuron projection (Fig. 5e); note that neuron projection processes were also significantly perturbed by the M489V variant on a WT background (e.g., Fig. 1d, e). To further characterize the impact of the PKC α mutation on these pathways, the phosphorylation of ERK1/2 was examined. It has been previously described that APP expression and exposure to oligomeric A β peptides enhance Ras/ERK signaling, increasing anomalous proliferation and subsequent neurodegeneration^{51,52}. Immunoblot analysis revealed increased phosphorylation of ERK1/2 in brain lysates from both the M489V non-tg-mice and the tg-AD mice compared to WT non tg-AD mice (Fig. 5f). This increase was also captured by the phosphoproteomics analysis (Fig. 5g). Thus, both the PKC α M489V mutation or the APP transgene enhance Erk signaling. Overall, phosphoproteomics analysis indicates that a slight enhancement in the catalytic activity of PKC α induces changes in protein phosphorylation in the brains of mice carrying the APP transgene at both 4.5 and 6 months of age. This altered signaling could lead to cell cycle deregulation, aberrant proliferative signaling and subsequent memory and learning disability at older ages.

Acceleration of impaired cognition in tg AD mouse with PKC M489V

The above studies indicate that the presence of the PKC α M489V AD variant is sufficient to impact the brain phosphoproteome at 3 months and learning ability in C57BL/6 mice at 12 months of age. To elucidate whether the presence of APP would aggravate or accelerate this effect on cognition, spatial learning and memory was assessed using the



Barnes maze test in mice harboring the PKC α M489V mutation (red) and WT littermate controls (blue) either without (WT and M489V) or with (WT tg-AD/M489V tg-AD) the *APP_{swE}* transgene at 4.5 (Fig. 6a), 6 (Fig. 6b) and 12 months of age (Fig. 6c). Introduction of this PKC α mutation onto the B6;SJL background without the *APP* transgene (non tg-AD) did not cause cognitive impairment at either of the early ages

tested (Figs. 6a, b), but deficits were apparent at 12 months of age (Fig. 6c). Thus, the PKC α mutation alone was sufficient to cause cognitive impairment in the non tg-AD mice, as reported for the C57BL/6 mice (Fig. 3d). The presence of the *APP_{swE}* transgene did not result in deficits in Barnes maze performance at the youngest age of 4.5 months in either WT tg-AD/M489V tg-AD mice (Fig. 6a), but it did produce

Fig. 5 | Phosphoproteomics analysis of brains from WT mice and mice harboring the PKC M489V mutation (red) on a B6;SJL background with the APP transgene carrying the Swedish mutation APP_{swe}. **a** Experimental design. Brains from WT (blue) or homozygous (red) mice with or without the APP_{swe} transgene at 4.5 and 6 months of age were subjected to phosphoproteomics analysis. 7574 proteins and 28,084 phosphopeptides were quantified in the standard proteomics and phosphoproteomics analyses, respectively. **b** Graphs showing the abundance of APP (left) and PKC α (right) detected in the proteomic analysis across all samples. Graphs depicts the mean \pm SD (p values obtained using a two-tailed Student's t test, $n = 3$ biologically independent samples). **c** Left. Immunoblot of brain lysates obtained from WT non tg-AD mice (lanes 1–5, dark blue) and tg-AD mice (lanes 6–10, light blue). Right. Relative phosphorylation represents the quantification of PKC substrates phospho-signal normalized to vinculin. Normalized data from the depicted western blot were plotted as average normalized intensity \pm SEM ($p = 0.0438$, using a two-tailed Student's t test). **d** Left: graph

showing the distribution of phosphopeptides from C9 Graph depicts the median \pm interquartile range (values of $p < 0.05$ using a two-tailed Student's t test, $n = 3$ biological independent samples). Right. GO enrichment analysis of C9 peptides using DAVID. **e** STRING analysis of proteins whose phosphopeptides were present in C9. Red represents proteins in the mTOR signaling pathway, green in the MAPK signaling pathway and blue represents proteins involved in neuron projection. **f** Left. Immunoblot of pERK1/2 (T202/Y204 for ERK1 and T185/Y187 for ERK2) and total ERK1/2 in brain lysates obtained from WT non-tg-AD (WT), M489V non tg-AD (M489V), WT tg-AD and M489V tg-AD mice at 6 months. Right. ERK1 (top) or ERK2 (bottom) phosphorylation reflects the normalized phospho-signal relative to total ERK. Data represent the average normalized intensity \pm SEM (ANOVA was used for statistical analysis, followed by post hoc two-tailed Student's t test). **g** Quantification of ERK phosphopeptides detected by phosphoproteomics in 6-month-old samples (mean \pm SD). Source data and uncropped blots for **c** and **f** are in the Source Data 1e.

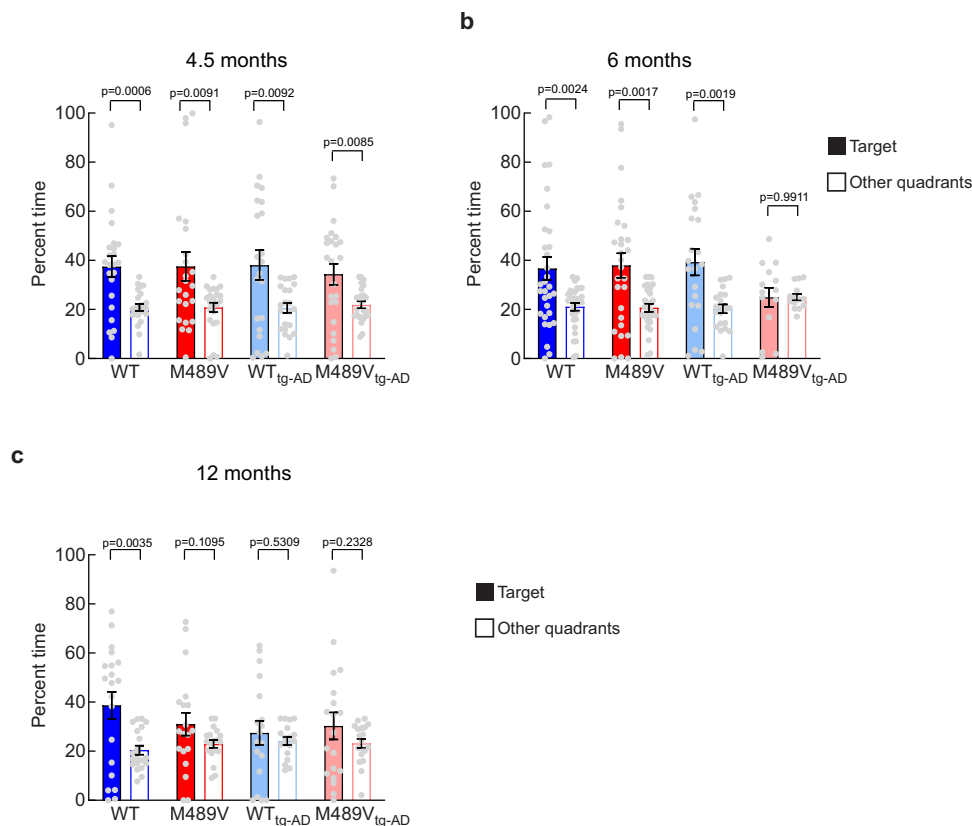


Fig. 6 | Impaired spatial learning in the Barnes maze test in PKC M489V mice + AD transgenic mouse. Percent time in the target quadrant (filled bars) vs. the average of the other quadrants (clear bars) in the probe test in separate groups of 4.5 (a), 6 (b) and 12 (c) month-old mice. Group sizes: 4.5-month (WT non tg-AD (WT): 12 males, 12 females, M489V non tg-AD (M489V): 11 males, 12 females, WT harboring the APP_{swe} transgene (WT tg-AD): 11 males, 11 females, M489V harboring the APP_{swe} transgene (M489V tg-AD): 12 males, 12 females), 6-month (WT: 15 males,

16 females, M489V: 12 males, 16 females, WT_{APP}: 10 males, 11 females, M489V_{APP}: 8 males, 6 females), 12 month (WT: 10 males, 10 females, M489V: 10 males, 9 females, WT_{APP}: 9 males, 9 females, M489V_{APP}: 5 males, 14 females). Error bars show standard error of the mean. No statistically significant sex differences were found. ANOVA was used for statistical analysis, followed by post hoc two-tailed Student's t test to determine the p values. Source data are provided in the Source Data 1e.

cognitive deficit at 12 months (Fig. 6c). Strikingly at 6 months, the tg-AD mice with WT PKC α (WT tg-AD) had normal cognition, but the presence of the M489V mutation (M489V tg-AD) abolished the ability of the mice to discriminate between the target quadrant (filled bars) and the other quadrants (open bars) (Fig. 6b). Thus, the PKC α M489V mutation accelerated the cognitive decline in the AD mouse model. It is important to highlight that neither M489V or M489V tg-AD mice showed reduced activity levels during the Barnes maze probe test or locomotor activity test, nor increased anxiety-like behavior in the light/dark test (Supp Fig. 5). Thus, this AD-associated mutation in PKC α , which enhances the catalytic activity of the enzyme by 30³⁴,

dramatically impaired cognition of mice at 6 months of age when paired with the APP_{swe} transgene (Fig. 6b) and was sufficient to affect learning and memory on its own at 12 months of age (Fig. 3d and Fig. 6c). These findings establish that 1] the M489V mutation in PKC α is sufficient, alone, to cause a behavioral defect in mice, and 2] the cognitive decline associated with APP_{swe} in this mouse line is accelerated in mice also harboring the PKC α mutation.

Increased PKC levels in human Alzheimer's disease brain
The above data indicate that enhanced PKC α signaling resulting from a rare, but highly penetrant variant of PKC α is sufficient to

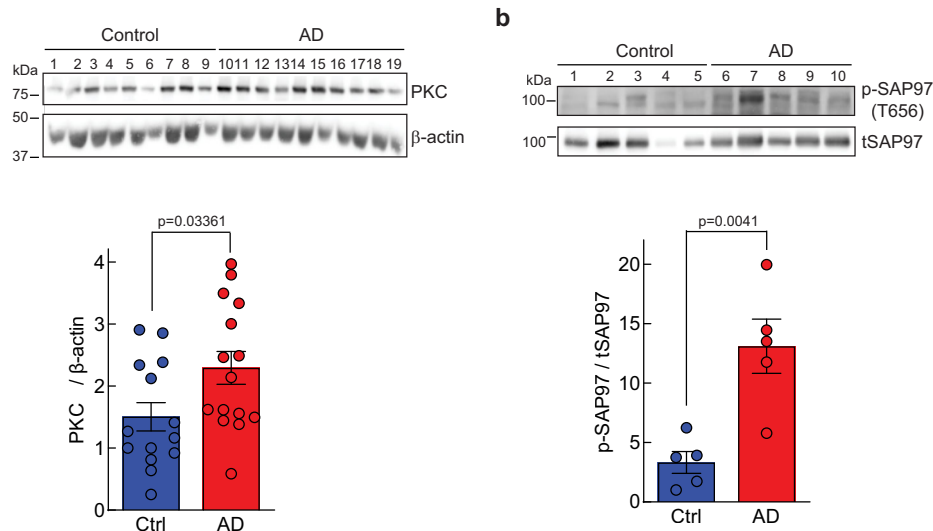


Fig. 7 | PKC levels and phosphorylation of SAP97 is increased in the frontal cortex of patients with Alzheimer's disease. **a** Western blot of lysates of frontal cortex obtained from nine brains (lanes 1–4, females; lanes 5–9, males) from control patients and nine brains (lanes 10–14, females; lanes 15–19, males) from AD patients. Western blots were probed with antibodies specific to total PKC α (top) and β -actin (bottom) as loading control. Graph depicts the quantification of the data in the western blot, including an additional 5 samples of each condition. **b** Western blot of lysates of frontal cortex obtained from five brains (lanes 1–2, males; lanes 3–5, females) from control patients and five brains (lanes 6–7, males; lanes 8–10,

females) from AD patients. Western blots were probed with antibodies specific to a known PKC phosphorylation site on SAP97 (Thr656) (Top) or to total SAP97 (Bottom). Graph depicts the quantification of the data in the western blot. **a, b** Bands were quantified using densitometry and the phospho-SAP97 signal was normalized to total SAP97 signal and PKC α signal was normalized to its β -actin loading control. Normalized data from the depicted western blots were plotted (Bottom) as average normalized intensity \pm SEM (p values were determined using unpaired two-tailed Student's t test). Source data and uncropped blots for figures **a** and **b** are in the Source Data file.

impair cognition. Given that elevated PKC signaling has been detected as one of the earliest events in the pathology of AD²⁹, we asked whether the steady-state levels of PKC α might be elevated in AD, resulting in enhanced signaling output. In this regard, the amount of PKC protein in cells regulates its signaling output²², with higher steady-state levels resulting in higher signaling output; for example, the related isozyme, PKC β II, has been shown to be haplo-insufficient in suppressing oncogenic signaling⁵³. Thus, we assessed the levels of PKC α protein in the frontal cortex of human brains from deceased patients with AD or control individuals by immunoblot as a measure of whether enhanced PKC α signaling output is associated with AD. This analysis revealed a statistically significant 20% increase in the steady-state levels of PKC α in the post-mortem brain of AD patients (Fig. 7a). Additionally, as another marker for PKC activation, we assessed the phosphorylation state of T656 on SAP97, a previously identified PKC α phosphorylation site³². Phosphorylation of T656 was increased by approximately four-fold in the brains from AD patients compared to control patients, consistent with higher PKC activity (Fig. 7b). These data reveal that PKC α is generally upregulated in human AD brain, resulting in enhanced substrate phosphorylation.

Discussion

Here we show that a highly penetrant, AD-associated mutation in PKC α is sufficient to cause impaired cognition in a mouse model. Furthermore, this mutation has a synergistic effect with enhanced APP production to exacerbate cognitive decline in the tg-AD mouse model. Thus, this mutation is not only sufficient to cause pathologies associated with AD, but likely does so by pathways separate from APP-induced AD. This mutant PKC α (M489V), which exhibits a 30% increase in catalytic rate, rewires the brain phosphoproteome, reduces the spine density in hippocampal neurons, enhances A β -dependent synaptic depression, and ultimately impairs cognition without impacting A β levels in the brain. Our work identifies PKC α inhibition as

a therapeutic strategy in AD which may be generally relevant as elevated PKC α protein, and hence signaling output, is associated with human AD patients.

Although PKC was originally discovered in the brain over four decades ago^{54,55}, it has only recently been recognized as an emerging biomarker and therapeutic target in neurodegeneration. Specifically, the advent of unbiased phosphoproteomic approaches and whole-genome sequencing puts the spotlight on PKC α , with mounting data pointing to a role in neurodegenerative diseases such as Alzheimer's. PKC isozymes are involved in numerous brain disorders such as glioblastoma, cerebral ischemia, addiction, and neurodegeneration^{56–59}, and their well-characterized effects on A β -mediated synaptic depression and phosphorylation of tau have been proposed mechanisms that lead to synaptic damage, neurotoxicity, and cognitive impairment^{3,4,59}. However, it is the unbiased approaches that provide the most compelling evidence for the critical role of PKC in maintaining normal brain function. A comprehensive phosphoproteome analysis by Tagawa et al.²⁹ revealed that PKC substrates account for over half of the core molecules that display increased phosphorylation in AD brains, a finding supported by subsequent phosphoproteomics studies identifying PKC as one of the main kinases activated in AD³⁰, and reporting increased phosphorylation of PKC α at Thr638⁶⁰, a quantitatively phosphorylated C-terminal site that serves as an indicator of PKC steady-state levels^{61,62}. Gain-of-function variants in PKC α segregating with affected family members in LOAD first drew specific attention to this conventional PKC isozyme²¹. In this study, we have leveraged one of these AD-associated rare variants, PKC α -M489V, to establish that a small increase in catalytic rate of PKC α is sufficient to drive cognitive decline in a mouse model. This particular variant was ideally suited for our study because the Met to Val substitution has no effect on auto-inhibition, on/off dynamics, or protein stability of PKC α , as established by biochemical and cellular analyses. Instead, the variant catalyzes 7 reactions per second, rather than the 5 reactions per second catalyzed by WT PKC α when in the active conformation³⁴. When introduced into a mouse model by genome editing, the steady-state levels of the

variant M489V PKC α are the same as that of the WT enzyme, validating the biochemical analysis that the mutation does not alter the stability of PKC α . Thus, this mutation provided an ideal model to interrogate whether a small enhancement in signaling output of PKC α is sufficient to cause cognitive decline. Strikingly, this small change in activity was sufficient to alter the brain phosphoproteome, reduce the spine density in hippocampal neurons, and impair cognition. Furthermore, analysis of post-mortem human brain revealed that, specific mutations aside, patients with AD generally have higher steady-state levels of PKC α . The steady-state levels of PKC are precisely set by diverse mechanisms, including stabilizing phosphorylations mediated by mTORC1 and PDK-1 and opposed by the quality control phosphatase PHLPP, as well as regulators such as Pin1, E3 ligases, and heat shock proteins⁶³. This suggests that not only are mutations in PKC α biomarkers for the disease, but the intrinsic set point of PKC α levels, controlled by diverse regulators, may also predict susceptibility to AD.

Gene Ontology analysis of the proteins whose phosphorylation increased in an M489V gene-dosage dependent manner (i.e. WT/WT < WT/M489V < M489V/M489V) identified components involved in the post-synaptic density and synapse processes. Proteins whose phosphorylation increased with increasing PKC α activity are likely downstream substrates of PKC whose phosphorylation modulates synaptic structure and function. PKC has previously been reported to phosphorylate numerous substrates to promote long term depression^{64,65}, including the dopamine transporter⁶⁶ and glutamate receptors such as α -amino-3-hydroxy-5-methyl-5-isoxazolepropionic acid (AMPA)-type glutamate receptors (AMPA) and N-Methyl-D-aspartic acid or N-Methyl-D-aspartate (NMDA)-type glutamate receptors (NMDARs)^{64,65,67}. Conversely, there was a group of peptides whose phosphorylation decreased in a gene-dosage-dependent manner. These are likely indirectly regulated downstream of PKC, either as a result of enhanced phosphatase activity or inhibited kinase activity directed at these substrates. Proteins in this group were involved in cytoskeleton and microtubule processes, supporting numerous studies on PKC regulating diverse cellular processes that culminate in cytoskeleton regulation. For example, phosphorylation of MARCKS and GAP43 by PKC promotes their translocation from the plasma membrane into the cytosol, triggering the depolarization and disruption of actin filaments^{68,69}. Additionally, PKC regulates tau phosphorylation, a microtubule-associated protein, and subsequently modulates the cytoskeleton dynamics in neurons⁷⁰⁻⁷². Taken together, increased PKC activity in the M489V mice may be disrupting the dynamics of microtubules and thus affecting the maintenance and formation of synapses in the brain.

Consistent with aberrations in the maintenance and formation of synapses, the M489V mice displayed a small but highly significant reduction in spine density in hippocampal neurons. PKC-catalyzed phosphorylation of MARCKS is well established to regulate dendritic spine morphology, with increased phosphorylation associated with reduced spine density^{73,74}. Furthermore, MARCKS phosphorylation has been proposed as a marker for degeneration, with elevated MARCKS phosphorylation preceding pathologies such as A β aggregation in several mouse models of AD²⁹. In our phosphoproteomic analysis of brains from WT and M489V mice, we observed an increase in MARCKS phosphorylation at Ser159/Ser163, consistent with previous studies that indicate that brains from mice harboring the M489V mutation in PKC α exhibit higher MARCKS phosphorylation³⁴. Taken together, the increased MARCKS phosphorylation resulting from the PKC α M489V variant may drive the neurite degeneration observed in the M489V mice. In correspondence with neurite degeneration, several studies have also correlated synapse density loss with memory deficits^{37,38}. Our behavioral studies support a correlation between spine density loss with neurodegeneration. Specifically, Barnes maze tests revealed that the M489V variant of PKC α alone, without the presence of APP, was able to induce cognitive impairment. These data indicate that

enhanced PKC α alone is sufficient to cause neurodegeneration. The finding that PKC α alone is able to cause impaired learning, with no impact of the variant on A β levels, suggests that PKC α may lead to neurodegeneration in an APP-independent manner. Alternatively, PKC α may act downstream of APP, accounting for why the variant accelerates APP-induced cognitive decline.

The molecular mechanisms by which enhanced PKC α activity leads to a cognitive deficit in a mouse model await elucidation. One clue to the puzzle is that PKC α transduces signaling downstream of A β . Previous studies have shown that A β fails to induce synaptic depression in hippocampal slices from PKC α knock-out animals²¹. Here we show that, conversely, A β -induced synaptic depression is exacerbated in animals with the activity-enhancing M489V variant. Furthermore, pharmacological and genetic approaches suggest that the synaptic depression effects of A β are mediated by PKC α acting on a protein scaffold via its PDZ ligand²¹. These results suggest that enhanced PKC α activity causes synaptic depression not only by increasing the phosphorylation and subsequent internalization of known membrane substrates such as GluR2⁶⁵, but also through the phosphorylation of its interaction partners such as SAP97³². The regulation of PDZ domain proteins by PKC may be an important mechanism to consider in the depressive effects of A β on synapses.

Our findings underscore the remarkable success of GWAS analysis in identifying functional AD variants that are tractable targets for therapy and can serve as biomarkers for the disease. As biomarkers, mutations in PKC α serve as a powerful diagnostic for disease susceptibility in AD, in the same way *BRCA* mutations are used as a diagnostic tool for breast cancer⁷⁵. Additionally, the steady-state levels of PKC α may serve as a diagnostic for disease susceptibility, as our analysis of post-mortem brains revealed that AD patients generally have higher steady-state levels of this enzyme. As a target, it is noteworthy that pharmacological inhibitors or aprinocarsen, a PKC α antisense oligonucleotide, which failed in clinical trials for cancer, could be repurposed for AD²⁸. Indeed, the use of specific PKC antisense oligonucleotides to reduce PKC levels is an attractive potential treatment of neurodegenerative diseases, as antisense strategies have been shown to successfully reduce LRRK2 protein levels in Parkinson's disease treatment⁷⁶, reduce superoxide dismutase 1 in amyotrophic lateral sclerosis⁷⁷, and improve clinical symptoms of patients with spinal muscular atrophy⁷⁸⁻⁸⁰. It should be noted that therapeutic strategies would only need to modestly reduce PKC activity, tuning activity down to homeostatic levels. The druggability of kinases, coupled to our detailed understanding of the molecular mechanisms of PKC, poise PKC α as an attractive target in AD.

Methods

All procedures involving animals were approved by The Scripps Research Institute's Institutional Animal Care and Usage Committee (IACUC) (Protocol number 09-0004) and the University of California San Diego IACUC (Protocol numbers S06288 and S11286), and met the guidelines of the National Institute of Health.

Mice

PKC -M489V mouse generation. C57BL/6NTac-*Prkca* mice containing the M489V mutation in *Prkca* were generated by Taconic Biosciences GmbH for Cure Alzheimer's Fund as previously described (Supp Fig. 1a)³⁴.

PPswe + PKC -M489V mouse generation. This mouse was generated by Taconic Biosciences GmbH for Cure Alzheimer's Fund by an initial intercross of C57BL/6NTac-*Prkca*M489V homozygous mice and the transgenic *APP_{swe}* mice (B6;SJL-Tg(APP_{SWE})2576Kha, model 1349, Taconic)⁵⁰. From this intercross, *Prkca*M489V heterozygous mice carrying the transgenic *APP_{swe}* mice (HET;APP) and *Prkca*M489V heterozygous mice not carrying the transgenic *APP_{swe}* (HET;NON-APP) were

obtained. Then, the offspring (HET;APP x HET;NON-APP) was intercrossed to generate the first cohort. Afterwards, HET;APP x HET;NON-APP breeding pairs were maintained to generate all the cohorts used for the experimental studies.

Housing conditions for the mice. Mice were group housed in a reverse light cycle room (lights off 8:00AM, on 8:00PM) with behavioral testing occurring in the early dark cycle (active phase), i.e. between 9:00AM and 1:00PM. The housing room was temperature (68–72 F) and humidity (44–61 %) controlled.

All procedures involving animals were approved by The Scripps Research Institute's Institutional Animal Care and Usage Committee (IACUC), and the University of California San Diego IACUC, and met the guidelines of the National Institute of Health detailed in the Guide for the Care and Use of Laboratory Animals⁸¹. The protocol numbers approved for these procedures are 09-0004, S06288, and S11286.

Behavioral tests

Barnes maze test. This is a spatial memory test^{82–84} sensitive to impaired hippocampal function⁸⁵. Mice learn to find an escape tunnel among 20 possibilities below an elevated, brightly lit and noisy platform using cues placed around the room. Spatial learning and memory are assessed across trials and then directly analyzed on the final probe trial in which the tunnel is removed and the time spent in each quadrant is determined; the percent time spent in the target quadrant (the one originally containing the escape box) is compared with the average percent time in the other three quadrants. This is a direct test of spatial memory as there is no potential for local cues to be used in the mouse's behavioral decision.

Locomotor activity test. Locomotor activity was measured in polycarbonate cages (42 × 22 × 20 cm) placed into frames (25.5 × 47 cm) mounted with two levels of photocell beams at 2 and 7 cm above the bottom of the cage (San Diego Instruments, San Diego, CA). These two sets of beams allowed for the recording of both horizontal (locomotion) and vertical (rearing) behavior. A thin layer of bedding material was applied to the bottom of the cage. Mice were tested for 120 min and data were collected in 5-minute intervals.

Light/dark test. The light/dark transfer procedure has been used to assess anxiety-like behavior in mice by capitalizing on the conflict between exploration of a novel environment and the avoidance of a brightly lit open field⁸⁶. The apparatus is a rectangular box made of Plexiglas divided by a partition into two environments. One compartment (14.5 × 27 × 26.5 cm) is dark (8–16 lux) and the other compartment (28.5 × 27 × 26.5 cm) is highly illuminated (400–600 lux) by a 60 W light source located above it. The compartments are connected by an opening (7.5 × 7.5 cm) located at floor level in the center of the partition. The time spent in the light compartment is used as a predictor of anxiety-like behavior, i.e., a greater amount of time in the light compartment is indicative of decreased anxiety-like behavior. Mice were placed in the dark compartment to start the 5-minute test.

ANOVA was used for the statistical analyses of behavioral results, followed by post hoc Student's *t* tests as appropriate to calculate the *p* values.

Electrophysiology

Organotypic slice cultures. Organotypic hippocampal slices were prepared from P5–P7 mice pups as previously described⁸⁷. Slice cultures were maintained by changing media every two days, and 18–24 h prior to electrophysiological experiments, slices were infected with Sindbis viruses to express the APP derived peptides CT84 and CT100 as previously described⁴⁸.

Electrophysiological recordings. Hippocampal organotypic slices were used for electrophysiological recordings shown in Fig. 7. Slices made from PKC α WT and M489V littermates were interleaved. Simultaneous whole-cell recordings were obtained from two neurons, one infected and one neighboring control CA1 pyramidal neurons under visual guidance using differential interference contrast and fluorescence microscopy. One stimulating electrode (contact Pt/Ir cluster electrodes (Frederick Haer)) was placed between 100 and 300 μ m down the apical dendrite. Whole-cell recordings were obtained with Axopatch-1D amplifiers (Molecular Devices) using 3–5 M Ω pipettes with an internal solution containing 115 mM cesium methanesulfonate, 20 mM CsCl, 10 mM HEPES, 2.5 mM MgCl₂, 4 mM Na₂ATP, 0.4 mM Na₃GTP, 10 mM sodium phosphocreatine (Sigma), and 0.6 mM EGTA (Amresco), at pH 7.25. External perfusion consisted of artificial cerebrospinal fluid containing 119 mM NaCl, 2.5 mM KCl, 4 mM CaCl₂, 4 mM MgCl₂, 26 mM NaHCO₃, 1 mM NaH₂PO₄, 11 mM glucose, 0.004 mM 2-chloroadenosine (Sigma), and 0.1 mM picrotoxin (Sigma) (pH 7.4), and gassed with 5% CO₂/95% O₂ at 27 °C. The AMPAR-mediated excitatory post-synaptic current (EPSC) was measured as peak inward current at a holding potential of -60 mV. Evoked responses were analyzed by averaging 30–100 sweeps using Igor Pro 4.04 software, blind to experimental conditions.

Mass spectrometry–phosphoproteomics

Murine brain tissue lysis. 3-month-old WT and homozygous M489V mice, and 4.5 and 6-month-old WT and homozygous M489V mice with or without the APP transgene were sacrificed and hemibrains were obtained and immediately snap-frozen. Frozen tissue was thawed on ice and homogenized via bead beating in a buffer containing 3% sodium dodecyl sulfate (SDS), 75 mM NaCl, 1 mM NaF, 1 mM β -glycerophosphate, 1 mM Na₃VO₄, 1 mM sodium pyrophosphate, 1 mM phenylmethylsulfonyl fluoride (PMSF), 1 \times complete EDTA-free protease inhibitor cocktail from Roche (Basel, Switzerland) and 50 mM HEPES, pH 8.5⁸⁸. Tissues were sonicated with a probe sonicator to ensure full lysis, insoluble cellular debris was removed via centrifugation (16,000 \times g, 10 min, 4 °C), and resultant supernatants were used for downstream processing.

Protein digestion. Proteins were denatured by addition of urea (4 M final concentration) then reduced with dithiothreitol (DTT) and alkylated with iodoacetamide (IAA)⁸⁹. Proteins were then precipitated with methanol/chloroform as previously described⁸⁹ and dried on a heat block at 56 °C. Dried protein pellets were resolubilized in 1 M urea in 50 mM HEPES, pH 8.5 for digestion in a two-step process (LysC for 16 h at room temperature (RT) followed by Trypsin for 6 h at 37 °C). Digests were acidified by addition of trifluoroacetic acid (TFA), and digested peptides were desalted with C18 Sep-Paks⁹⁰. Desalted peptides were dried, resuspended in 50% acetonitrile/5% formic acid and quantified using the Pierce Quantitative Colorimetric Peptide Assay. Peptides from matched samples were aliquoted for both standard proteomics (50 μ g) and phosphoproteomics (4 mg) and lyophilized.

Phosphopeptide enrichment. Phosphopeptides were enriched by TiO₂ beads as previously described^{91,92}. Peptides were resuspended in binding buffer (2 M lactic acid, 50% acetonitrile) and incubated with TiO₂ beads that were pre-washed 1 \times with binding buffer, 1 \times with elution buffer (50 mM KH₂PO₄, pH 10) and 2 \times with binding buffer. Enrichment was conducted at a ratio of 1:4 (peptides:beads) for 1 h at RT. Peptide:bead complexes were washed 3 \times with binding buffer and 3 \times with wash buffer (50% acetonitrile/0.1% trifluoroacetic acid) to remove non-specific binding. Phosphopeptides were then eluted from the beads using 2 \times 5 min incubations in elution buffer while vortexing at RT. Enriched phosphopeptides were desalted and lyophilized prior to TMT labeling.

Tandem mass tag (TMT) labeling. For both standard and phosphoproteomics, peptides were labeled for quantitation using TMT 10-plex reagents^{93,94}. TMT reagents were resuspended in dry acetonitrile to a concentration of 20 $\mu\text{g}/\mu\text{l}$. Lyophilized peptides were resuspended in 30 μl acetonitrile in 200 mM HEPES, pH 8.5 and mixed with 8 μl of the appropriate TMT reagent. The TMT126 reagent in each 10-plex was reserved for a bridge channel, which consists of an equal amount of each sample pooled together, and the remaining TMT reagents were used to label individual sample digests. The bridge channel served to control for experimental variation between individual 10-plex experiments. TMT labeling was conducted for one hour at RT, quenched with 9 μl of 5% hydroxylamine for 15 min at RT, then acidified with 50 μl of 1% TFA and pooled. The multiplexed samples were desalted as above to remove unreacted TMT reagents, then lyophilized.

Basic reverse-phase liquid chromatography fractionation (bRPLC). Multiplexed samples were fractionated by bRPLC with fraction combining as previously described⁹⁰. Samples were resuspended in 5% formic acid in 5% acetonitrile and separated on a 4.6 mm \times 250 mm C18 column using an Ultimate 3000 HPLC into 96 fractions. The resultant fractions were then combined into 24 fractions and lyophilized prior to LC-MS3 analysis.

LC-MS3 analysis. Samples were resuspended in 5% acetonitrile/5% formic acid and separated on an Easy-nanoLC 1000 in-line with an Orbitrap Fusion Tribrid mass spectrometer. Samples were loaded onto a glass capillary column (length: 30 cm, I.D. 100 μm , O.D. 350 μm) pulled and packed in-house with 0.5 cm of 5 μm C4 resin followed by 0.5 cm of 3 μm C18 resin, with the remainder of the column packed with 1.8 μm of C18 resin. Once the sample was loaded, peptides were eluted using a gradient ranging from 11–30% acetonitrile in 0.125% formic acid over 180 min at a flow rate of 300 nL/min. The column was heated to 60 $^{\circ}\text{C}$ and electrospray ionization was achieved by applying of 2000 V of electricity through a T-junction at the inlet of the column.

All data were centroided and collected in data-dependent mode. An MS1 survey scan was performed over a mass to charge (m/z) range of 500–1200 at a resolution of 60,000 in the Orbitrap. Automatic gain control (AGC) was set to 200,000 with a maximum ion inject time of 100 ms and a lower threshold for ion intensity of 50,000. Ions selected for MS2 analysis were isolated with a width of 0.5 m/z in the quadrupole and fragmented using collision-induced dissociation (CID) with a normalized collision energy of 30%. Ion fragments were detected in the linear ion trap with the rapid scan rate setting with an AGC of 10,000 and a maximum inject time of 35 ms. MS3 analysis was conducted using the synchronous precursor selection (SPS) to simultaneously isolate 10 ions (regular proteomics) or 3 ions (phosphoproteomics) to maximize TMT sensitivity⁹⁵. TMT reporter ions were fragmented off the peptides with higher energy collision induced dissociation (normalized energy of 50%) and MS3 fragment ions were analyzed in the Orbitrap at a resolution of 60,000. The AGC was set to 50,000 with a maximum ion injection time of 150 ms. MS2 ions 40 m/z below and 15 m/z above the MS1 precursor ion were excluded from MS3 selection.

Data processing and analysis. Resultant mass spectrometry data files were analyzed using Proteome Discoverer 2.1. MS2 spectra were queried against the Uniprot human protein database (downloaded: 05/2017) using the Sequest search algorithm⁹⁶. A decoy search was also conducted with sequences in reverse to estimate FDR^{97–99}. A mass tolerance of 50 ppm was used for MS1 spectra and a tolerance of 0.6 Da was used for MS2 spectra. TMT 10-plex reagents on lysine and peptide n-termini and carbamidomethylation of cysteines were included as static modifications. Oxidation of methionine and, for the phosphoproteomics experiments, phosphorylation of serine, threonine, and tyrosine residues, were also included in the search parameters as variable modifications. The target-decoy strategy was used to filter

results to a 1% FDR at the peptide and protein levels^{97–99}. Reporter ion intensities extracted from MS3 spectra were used for quantitative analysis. For regular proteomics, protein-level abundance values were calculated by summing signal-to-noise values for all peptides per protein meeting the specified filters. Data were normalized as previously described¹⁰⁰. Phosphopeptide abundance was normalized similarly, except quantitation was summed to the unique phosphopeptide level then normalized to the total protein level. Phosphosite localization was performed using the PhosphoRS node within Proteome Discoverer. The PTMphinder R package was used to localize phosphorylated residues in the context of full-length proteins¹⁰¹. The significant peptides were determined via “pi score” which combines t test p values and fold-changes into a single metric¹⁰² (PAPER XIAO 2014, Bioinformatics). We used a pi score that corresponds to an alpha of <0.05 as a cutoff for significant proteins. The t test used to calculate the pi score was two-sided and not corrected for multiple hypotheses. Prior to direct statistical comparisons, K-means clustering was used to group all quantified phosphopeptides with similar expression profiles. Gene ontology analysis was used to identify enriched pathways in clustered phosphopeptides through the DAVID server (<https://david.ncifcrf.gov/>)^{103,104}. K-means clustering was used to group all quantified phosphopeptides with similar expression profiles, prior to direct statistical comparisons. STRING-db (v11.0) was utilized to generate functional protein association networks of proteins of interest¹⁰⁵. Connections were limited to high confidence (0.7) with a maximum of 20 connections for the second shell. First shell of interactions was restricted to the query only.

Spine density analysis

Brain slice preparation. Mice were deeply anesthetized with ketamine, and perfused with 0.9% w/v Sodium Chloride, then perfused with 4% paraformaldehyde (PFA) in phosphate buffer (PB). The brain tissues were removed and post-fixed in 4% PFA in PB for 30 min. Using a vibratome, 100 μm coronal sections were sliced and stored in 1 \times dPBS. Alexa Fluor[®] 594 Hydrazide (Thermo Fisher Scientific A10438) was injected into CA1 pyramidal neurons to follow neuronal projections. Injected slices were post-fixed for 15 min on 4% PFA in PB prior to mounting with Aqua-Poly/Mount (Polysciences Inc. 18606-20).

Confocal microscopy and dendritic spine analysis. Immunofluorescent images of hippocampal neurons were acquired with a Leica DMI6000 inverted microscope equipped with a Yokogawa Nipkow Spinning disk confocal head, an Orca ER High-Resolution black and white cooled CCD camera (6.45 m^2/pixel at 1 \times) (Hamamatsu), Plan ApoChromat 63 \times /1.4 numerical aperture objective, and Andor 100 mW 561 nm laser. Confocal z-stacks were acquired in all experiments and all imaging was acquired in the dynamic range of 8-bit acquisition (0–255 pixel intensity units, respectively) with Velocity v6.1.1 (PerkinElmer) imaging software. Imaged dendrites from one secondary dendrite per cell (after 1 branch) at a distance of 40–80 μm from the soma were straightened using ImageJ v1.41o. We estimated spine density as the number of manually counted spines (length ≥ 2 experimental conditions). Statistical significance was determined using unpaired Student's t -tests.

Western blot analysis

Fresh frozen post-mortem human brains (frontal cortex) from longitudinally followed and characterized individuals were provided by the ADRC Neuropathology Core at UCSD. Mice were euthanized and brain samples were obtained and snap-frozen immediately after collection. All procedures involving animals were approved by The Scripps Research Institute's Institutional Animal Care and Usage Committee (IACUC) and the UCSD IACUC, and met the guidelines of the National Institute of Health detailed in the Guide for the Care and Use of Laboratory Animals⁸¹.

Frozen brain tissues were lysed and homogenized in a Dounce tissue grinder with RIPA buffer (50 mM Tris, pH 7.4, 1% Triton X-100, 1% NaDOC, 0.1% SDS, 150 mM NaCl, 2 mM EDTA, 10 mM NaF, 1 mM DTT, 1 mM Na₃VO₄, 1 mM PMSF, 50 µg/mL leupeptin, 1 µM microcystin, and 2 mM benzamide). Homogenates were sonicated and protein was quantified using a BCA protein assay kit (Thermo Fisher Scientific). Fifty micrograms of protein were separated by standard SDS/PAGE and transferred to PVDF membranes (BioRad). Membranes were blocked with 5% BSA or 5% milk for one hour at room temperature and analyzed by immunoblotting with specific antibodies. Detection of immunoreactive bands was performed via chemiluminescence on a FluorChemQ imaging system (Alpha Innotech). Analyses were performed using the AlphaView SA, version 3.4.0 software.

Antibodies: anti-PKCα antibody (610108, clone 3/PKCα, used at 1:1,000 dilution) was from BD Transduction Laboratories. β-Actin antibody was purchased from Sigma-Aldrich (A2228, clone AC-74, used at 1:20,000 dilution), total SAP97 was from Enzo Life Sciences (ADI-VAM-PS005, clone RPI 197.4, used at 1:1000 dilution), phospho-MARCKS (sc-12971-R) and total MARCKS (sc-6454) were obtained from Santa Cruz Biotechnology (both used at a 1:250 dilution). GAPDH (2118, clone C1410), vinculin (4650), phospho-(Ser) PKC substrate (2261S), phospho-ERK1/2 (9101) and total ERK1/2 (9102) antibodies were purchased from Cell Signaling Technology, and were used at a 1:1000 dilution. The pSAP97 (T656) antibody was custom made by NeomPS by immunizing rabbits with an Ac-CKERARKL-T(PO3H2)-VKFN-NH2 peptide that was conjugated to keyhole limpet hemocyanin and was affinity-purified using the phosphopeptide antigen, as described and characterized in O'Neill *et al.*³². It was used at a 1:1000 dilution.

Statistical analysis

For the statistical analyses of behavioral results, analysis of variance (ANOVA) was used followed by post hoc Student's *t* tests as appropriate. For spine density statistical analysis and immunoblots statistical analysis unpaired Student's *t* tests were used. To assess statistical significance of dual-patch recordings, two-way ANOVA was used followed with Newman-Keuls multiple comparison post hoc test (to compare CT100-induced depression in WT versus M489V mice). Paired *t* tests were used to assess CT100-induced depression in dual-recordings performed simultaneously in WT and M489V mice. Data was graphed using GraphPad Prism 9.

Reporting summary

Further information on research design is available in the Nature Portfolio Reporting Summary linked to this article.

Data availability

The MS proteomics data generated for this manuscript, including annotated spectra, have been deposited onto the ProteomeXchange archive through MassIVE under the following identifiers: PKC-M489V 3 months old mice, C57BL/6N background (ProteomeXchange: [PXD029092](https://proteomecentral.proteomex.org/submitter/massive/029092)), PKC-M489V 4.5 and 6 months old mice, APP transgenic background (ProteomeXchange: [PXD029093](https://proteomecentral.proteomex.org/submitter/massive/029093)). The processed MS proteomics are available within the Dataset 1 and Dataset 2 files. All other data needed to evaluate the conclusions in the paper are contained within the manuscript or the Supplementary Information file and the Source Data file. Source data are provided with this paper.

References

- Mattson, M. P. Pathways towards and away from Alzheimer's disease. *Nature* **430**, 631–639 (2004).
- Long, J. M., Holtzman, D. M. Alzheimer disease: an update on pathobiology and treatment strategies. *Cell* **179**, 312–339 (2019).
- Ittner, L. M., Gotz, J. Amyloid-beta and tau—a toxic pas de deux in Alzheimer's disease. *Nat. Rev. Neurosci.* **12**, 65–72 (2011).
- Busche, M. A., Hyman, B. T. Synergy between amyloid-beta and tau in Alzheimer's disease. *Nat. Neurosci.* **23**, 1183–1193 (2020).
- Müller, U. C., Zheng, H. Physiological functions of APP family proteins. *Cold Spring Harb. Perspect. Med.* **2**, a006288 (2012).
- Haass, C., Kaether, C., Thinakaran, G., Sisodia, S. Trafficking and proteolytic processing of APP. *Cold Spring Harb. Perspect. Med.* **2**, a006270 (2012).
- Haass, C., Selkoe, D. J. Soluble protein oligomers in neurodegeneration: lessons from the Alzheimer's amyloid beta-peptide. *Nat. Rev. Mol. Cell Biol.* **8**, 101–112 (2007).
- Mullan, M. *et al.* A pathogenic mutation for probable Alzheimer's disease in the APP gene at the N-terminus of beta-amyloid. *Nat. Genet.* **1**, 345–347 (1992).
- Sherrington, R. *et al.* Cloning of a gene bearing missense mutations in early-onset familial Alzheimer's disease. *Nature* **375**, 754–760 (1995).
- Levy-Lahad, E. *et al.* Candidate gene for the chromosome 1 familial Alzheimer's disease locus. *Science* **269**, 973–977 (1995).
- Rogaev, E. I. *et al.* Familial Alzheimer's disease in kindreds with missense mutations in a gene on chromosome 1 related to the Alzheimer's disease type 3 gene. *Nature* **376**, 775–778 (1995).
- Sims, R., Hill, M., Williams, J. The multiplex model of the genetics of Alzheimer's disease. *Nat. Neurosci.* **23**, 311–322 (2020).
- Strittmatter, W. J. *et al.* Apolipoprotein E: high-avidity binding to beta-amyloid and increased frequency of type 4 allele in late-onset familial Alzheimer disease. *Proc. Natl Acad. Sci. USA* **90**, 1977–1981 (1993).
- Strittmatter, W. J. *et al.* Binding of human apolipoprotein E to synthetic amyloid beta peptide: isoform-specific effects and implications for late-onset Alzheimer disease. *Proc. Natl Acad. Sci. USA* **90**, 8098–8102 (1993).
- Corder, E. H. *et al.* Gene dose of apolipoprotein E type 4 allele and the risk of Alzheimer's disease in late onset families. *Science* **261**, 921–923 (1993).
- Prokopenko, D. *et al.* Whole-genome sequencing reveals new Alzheimer's disease-associated rare variants in loci related to synaptic function and neuronal development. *Alzheimers Dement.* (2021).
- Jonsson, T. *et al.* Variant of TREM2 associated with the risk of Alzheimer's disease. *N. Engl. J. Med.* **368**, 107–116 (2013).
- Ulland, T. K., Colonna, M. TREM2—a key player in microglial biology and Alzheimer disease. *Nat. Rev. Neurol.* **14**, 667–675 (2018).
- Guerreiro, R. *et al.* TREM2 variants in Alzheimer's disease. *N. Engl. J. Med.* **368**, 117–127 (2013).
- Sims, R. *et al.* Rare coding variants in PLCG2, ABI3, and TREM2 implicate microglial-mediated innate immunity in Alzheimer's disease. *Nat. Genet.* **49**, 1373–1384 (2017).
- Alfonso, S. I. *et al.* Gain-of-function mutations in protein kinase Calpha (PKCalpha) may promote synaptic defects in Alzheimer's disease. *Sci. Signal.* **9**, ra47 (2016).
- Newton, A. C. Protein kinase C: perfectly balanced. *Crit. Rev. Biochem. Mol. Biol.* **53**, 208–230 (2018).
- Nishizuka, Y. *et al.* A role of calcium in the activation of a new protein kinase system. *Adv. Cycl. Nucleotide Res.* **9**, 209–220 (1978).
- Takai, Y., Kishimoto, A., Kikkawa, U., Mori, T., Nishizuka, Y. Unsaturated diacylglycerol as a possible messenger for the activation of calcium-activated, phospholipid-dependent protein kinase system. *Biochem. Biophys. Res Commun.* **91**, 1218–1224 (1979).
- Baf, T. R., Van, A. N., Zhao, W., Mills, G. B., Newton, A. C. Protein kinase C quality control by phosphatase PHLPP1 unveils loss-of-function mechanism in cancer. *Mol. Cell* **74**, 378–392 e375 (2019).

26. Tovell, H. Newton, A. C. PHLPPing the balance: restoration of protein kinase C in cancer. *Biochem J.* **478**, 341–355 (2021).
27. Newton, A. C. Brognard, J. Reversing the paradigm: protein kinase C as a tumor suppressor. *Trends Pharmacol. Sci.* **38**, 438–447 (2017).
28. Zhang, L. L. et al. The protein kinase C (PKC) inhibitors combined with chemotherapy in the treatment of advanced non-small cell lung cancer: meta-analysis of randomized controlled trials. *Clin. Transl. Oncol.* **17**, 371–377 (2015).
29. Tagawa, K. et al. Comprehensive phosphoproteome analysis unravels the core signaling network that initiates the earliest synapse pathology in preclinical Alzheimer's disease brain. *Hum. Mol. Genet.* **24**, 540–558 (2015).
30. Morshed, N. et al. Quantitative phosphoproteomics uncovers dysregulated kinase networks in Alzheimer's disease. *Nat. Aging* **1**, 550–565 (2021).
31. Alfonso, S. et al. Synapto-depressive effects of amyloid beta require PICK1. *Eur. J. Neurosci.* **39**, 1225–1233 (2014).
32. O'Neill, A. K. et al. Protein kinase C α promotes cell migration through a PDZ-dependent interaction with its novel substrate discs large homolog 1 (DLG1). *J. Biol. Chem.* **286**, 43559–43568 (2011).
33. Staudinger, J., Lu, J. Olson, E. N. Specific interaction of the PDZ domain protein PICK1 with the COOH terminus of protein kinase C- α . *J. Biol. Chem.* **272**, 32019–32024 (1997).
34. Callender, J. A. et al. Protein kinase C α gain-of-function variant in Alzheimer's disease displays enhanced catalysis by a mechanism that evades down-regulation. *Proc. Natl Acad. Sci. USA* **115**, E5497–E5505 (2018).
35. Runge, K., Cardoso, C. de Chevigny, A. Dendritic spine plasticity: function and mechanisms. *Front. synaptic Neurosci.* **12**, 36 (2020).
36. Pchitskaya, E. Bezprozvanny, I. Dendritic spines shape analysis-classification or clusterization? perspective. *Front. synaptic Neurosci.* **12**, 31 (2020).
37. Gipson, C. D. Olive, M. F. Structural and functional plasticity of dendritic spines - root or result of behavior? *Genes Brain Behav.* **16**, 101–117 (2017).
38. Durand, G. M., Kovalchuk, Y. Konnerth, A. Long-term potentiation and functional synapse induction in developing hippocampus. *Nature* **381**, 71–75 (1996).
39. Borbély, E. et al. Simultaneous changes of spatial memory and spine density after intrahippocampal administration of brilliant $\alpha\beta 1-42$ to the rat brain. *BioMed. Res. Int.* **2014**, 345305 (2014).
40. Faizi, M. et al. Thy1-hAPP(Lond/Swe+) mouse model of Alzheimer's disease displays broad behavioral deficits in sensorimotor, cognitive and social function. *Brain Behav.* **2**, 142–154 (2012).
41. Masters, C. L. et al. Amyloid plaque core protein in Alzheimer's disease and Down syndrome. *Proc. Natl Acad. Sci. USA* **82**, 4245–4249 (1985).
42. De Strooper, B. Annaert, W. Proteolytic processing and cell biological functions of the amyloid precursor protein. *J. Cell Sci.* **113**(Pt 11), 1857–1870 (2000).
43. Reinders, N. R. et al. Amyloid-beta effects on synapses and memory require AMPA receptor subunit GluA3. *Proc. Natl Acad. Sci. USA* **113**, E6526–E6534 (2016).
44. Leitges, M., Kovac, J., Plomann, M. Linden, D. J. A unique PDZ ligand in PKC α confers induction of cerebellar long-term synaptic depression. *Neuron* **44**, 585–594 (2004).
45. Kamenetz, F. et al. APP processing and synaptic function. *Neuron* **37**, 925–937 (2003).
46. Wilcox, K. C., Lacor, P. N., Pitt, J. Klein, W. L. A β oligomer-induced synapse degeneration in Alzheimer's disease. *Cell. Mol. Neurobiol.* **31**, 939–948 (2011).
47. Wei, W. et al. Amyloid beta from axons and dendrites reduces local spine number and plasticity. *Nat. Neurosci.* **13**, 190–196 (2010).
48. Dore, K. et al. PSD-95 protects synapses from β -amyloid. *Cell Rep.* **35**, 109194 (2021).
49. Kessels, H. W., Nabavi, S. Malinow, R. Metabotropic NMDA receptor function is required for β -amyloid-induced synaptic depression. *Proc. Natl Acad. Sci. USA* **110**, 4033–4038 (2013).
50. Hsiao, K. et al. Correlative memory deficits, A β elevation, and amyloid plaques in transgenic mice. *Science* **274**, 99–102 (1996).
51. Chaput, D., Kirouac, L. H., Bell-Temin, H., Stevens, S. M. Jr. Padmanabhan, J. SILAC-based proteomic analysis to investigate the impact of amyloid precursor protein expression in neuronal-like B103 cells. *Electrophoresis* **33**, 3728–3737 (2012).
52. Kirouac L., Rajic A. J., Cribbs D. H., Padmanabhan J. Activation of Ras-ERK signaling and GSK-3 by amyloid precursor protein and amyloid beta facilitates neurodegeneration in Alzheimer's disease. *eNeuro* **4**, ENEURO.0149-16.2017 (2017).
53. Antal, C. E. et al. Cancer-associated protein kinase C mutations reveal kinase's role as tumor suppressor. *Cell* **160**, 489–502 (2015).
54. Takai, Y., Kishimoto, A., Inoue, M. Nishizuka, Y. Studies on a cyclic nucleotide-independent protein kinase and its proenzyme in mammalian tissues. I. Purification and characterization of an active enzyme from bovine cerebellum. *J. Biol. Chem.* **252**, 7603–7609 (1977).
55. Inoue, M., Kishimoto, A., Takai, Y. Nishizuka, Y. Studies on a cyclic nucleotide-independent protein kinase and its proenzyme in mammalian tissues. II. Proenzyme and its activation by calcium-dependent protease from rat brain. *J. Biol. Chem.* **252**, 7610–7616 (1977).
56. Parker, P. J., Justilien, V., Riou, P., Lynch, M. Fields, A. P. Atypical protein kinase C as a human oncogene and therapeutic target. *Biochem. Pharm.* **88**, 1–11 (2014).
57. Bright, R. Mochly-Rosen, D. The role of protein kinase C in cerebral ischemic and reperfusion injury. *Stroke* **36**, 2781–2790 (2005).
58. Hodge, C. W. et al. Supersensitivity to allosteric GABA(A) receptor modulators and alcohol in mice lacking PKCepsilon. *Nat. Neurosci.* **2**, 997–1002 (1999).
59. Callender J. A., Newton A. C. Conventional protein kinase C in the brain: 40 years later. *Neuronal Signal.* **1**, NS20160005 (2017).
60. Bai, B. et al. Deep multilayer brain proteomics identifies molecular networks in Alzheimer's disease progression. *Neuron* **106**, 700 (2020).
61. Newton, A. C. Protein kinase C: poised to signal. *Am. J. Physiol. Endocrinol. Metab.* **298**, E395–E402 (2010).
62. Lorden, G. Newton, A. C. Conventional protein kinase C in the brain: repurposing cancer drugs for neurodegenerative treatment. *Neuronal Signal.* **5**, NS20210036 (2021).
63. Baf, T. R. Newton, A. C. Protein kinase C: release from quarantine by mTORC2. *Trends Biochem. Sci.* **47**, 518–530 (2022).
64. Boehm, J. et al. Synaptic incorporation of AMPA receptors during LTP is controlled by a PKC phosphorylation site on GluR1. *Neuron* **51**, 213–225 (2006).
65. Chung, H. J., Xia, J., Scannevin, R. H., Zhang, X. Huganir, R. L. Phosphorylation of the AMPA receptor subunit GluR2 differentially regulates its interaction with PDZ domain-containing proteins. *J. Neurosci.* **20**, 7258–7267 (2000).
66. Foster, J. D. Vaughan, R. A. Phosphorylation mechanisms in dopamine transporter regulation. *J. Chem. Neuroanat.* **83–84**, 10–18 (2017).
67. Kim, C. H., Braud, S., Isaac, J. T. Roche, K. W. Protein kinase C phosphorylation of the metabotropic glutamate receptor mGluR5

- on Serine 839 regulates Ca²⁺ oscillations. *J. Biol. Chem.* **280**, 25409–25415 (2005).
68. Hartwig, J. H. et al. MARCKS is an actin filament crosslinking protein regulated by protein kinase C and calcium-calmodulin. *Nature* **356**, 618–622 (1992).
69. Kim, J., Blackshear, P. J., Johnson, J. D., McLaughlin, S. Phosphorylation reverses the membrane association of peptides that correspond to the basic domains of MARCKS and neuromodulin. *Biophys. J.* **67**, 227–237 (1994).
70. Correas, I., Díaz-Nido, J., Avila, J. Microtubule-associated protein tau is phosphorylated by protein kinase C on its tubulin binding domain. *J. Biol. Chem.* **267**, 15721–15728 (1992).
71. Wang, Y., Mandelkow, E. Tau in physiology and pathology. *Nat. Rev. Neurosci.* **17**, 5–21 (2016).
72. Isagawa, T. et al. Dual effects of PKNalpha and protein kinase C on phosphorylation of tau protein by glycogen synthase kinase-3beta. *Biochem. Biophys. Res Commun.* **273**, 209–212 (2000).
73. Fujita, K. et al. Ser46-phosphorylated MARCKS is a marker of neurite degeneration at the pre-aggregation stage in PD/DLB pathology. *eNeuro* **5**, ENEURO.0217-18.2018 (2018).
74. Calabrese, B., Halpain, S. Essential role for the PKC target MARCKS in maintaining dendritic spine morphology. *Neuron* **48**, 77–90 (2005).
75. Hall, J. M. et al. Linkage of early-onset familial breast cancer to chromosome 17q21. *Science* **250**, 1684–1689 (1990).
76. Zhao, H. T. et al. LRRK2 antisense oligonucleotides ameliorate alpha-synuclein inclusion formation in a Parkinson's disease mouse model. *Mol. Ther. Nucleic Acids* **8**, 508–519 (2017).
77. Smith, R. A. et al. Antisense oligonucleotide therapy for neurodegenerative disease. *J. Clin. Invest.* **116**, 2290–2296 (2006).
78. Darras, B. T. et al. An integrated safety analysis of infants and children with symptomatic spinal muscular atrophy (SMA) treated with nusinersen in seven clinical Trials. *CNS Drugs* **33**, 919–932 (2019).
79. De Vivo, D. C. et al. Nusinersen initiated in infants during the presymptomatic stage of spinal muscular atrophy: Interim efficacy and safety results from the Phase 2 NURTURE study. *Neuromuscul. Disord.* **29**, 842–856 (2019).
80. Bennett, C. F., Kordasiewicz, H. B., Cleveland, D. W. Antisense drugs make sense for neurological diseases. *Annu. Rev. Pharm. Toxicol.* **61**, 831–852 (2021).
81. National Research Council (US). Guide for the Care and Use of Laboratory Animals. 8th Edition. Washington, DC: National Academies Press (US), (2011).
82. Barnes, C. A. Memory deficits associated with senescence: a neurophysiological and behavioral study in the rat. *J. Comp. Physiol. Psychol.* **93**, 74–104 (1979).
83. Bach, M. E., Hawkins, R. D., Osman, M., Kandel, E. R., Mayford, M. Impairment of spatial but not contextual memory in CaMKII mutant mice with a selective loss of hippocampal LTP in the range of the theta frequency. *Cell* **81**, 905–915 (1995).
84. Holmes, A., Wrenn, C. C., Harris, A. P., Thayer, K. E., Crawley, J. N. Behavioral profiles of inbred strains on novel olfactory, spatial and emotional tests for reference memory in mice. *Genes Brain Behav.* **1**, 55–69 (2002).
85. Paylor, R., Zhao, Y., Libbey, M., Westphal, H., Crawley, J. N. Learning impairments and motor dysfunctions in adult Lhx5-deficient mice displaying hippocampal disorganization. *Physiol. Behav.* **73**, 781–792 (2001).
86. Crawley, J. N. Behavioral phenotyping of transgenic and knockout mice: experimental design and evaluation of general health, sensory functions, motor abilities, and specific behavioral tests. *Brain Res.* **835**, 18–26 (1999).
87. Stoppini, L., Buchs, P. A., Muller, D. A simple method for organotypic cultures of nervous tissue. *J. Neurosci. Methods* **37**, 173–182 (1991).
88. Wozniak, J. M. et al. Molecular dissection of Chagas induced cardiomyopathy reveals central disease associated and druggable signaling pathways. *PLoS Negl. Trop. Dis.* **14**, e0007980 (2020).
89. Haas, W. et al. Optimization and use of peptide mass measurement accuracy in shotgun proteomics. *Mol. Cell. Proteom.* **5**, 1326–1337 (2006).
90. Tolonen, A. C., Haas, W. Quantitative proteomics using reductive dimethylation for stable isotope labeling. *Journal of visualized experiments: JoVE*, 51416 (2014).
91. Huttlin, E. L. et al. A tissue-specific atlas of mouse protein phosphorylation and expression. *Cell* **143**, 1174–1189 (2010).
92. Lin, Y. et al. Phosphoproteomic analysis of protease-activated receptor-1 biased signaling reveals unique modulators of endothelial barrier function. *Proc. Natl Acad. Sci. USA* **117**, 5039–5048 (2020).
93. McAlister, G. C. et al. Increasing the multiplexing capacity of TMTs using reporter ion isotopologues with isobaric masses. *Anal. Chem.* **84**, 7469–7478 (2012).
94. Thompson, A. et al. Tandem mass tags: a novel quantification strategy for comparative analysis of complex protein mixtures by MS/MS. *Anal. Chem.* **75**, 1895–1904 (2003).
95. McAlister, G. C. et al. MultiNotch MS3 enables accurate, sensitive, and multiplexed detection of differential expression across cancer cell line proteomes. *Anal. Chem.* **86**, 7150–7158 (2014).
96. Eng, J. K., McCormack, A. L., Yates, J. R. An approach to correlate tandem mass spectral data of peptides with amino acid sequences in a protein database. *J. Am. Soc. Mass Spectrom.* **5**, 976–989 (1994).
97. Elias, J. E., Haas, W., Faherty, B. K., Gygi, S. P. Comparative evaluation of mass spectrometry platforms used in large-scale proteomics investigations. *Nat. methods* **2**, 667–675 (2005).
98. Gupta, N., Pevzner, P. A. False discovery rates of protein identifications: a strike against the two-peptide rule. *J. Proteome Res.* **8**, 4173–4181 (2009).
99. Elias, J. E., Gygi, S. P. Target-decoy search strategy for increased confidence in large-scale protein identifications by mass spectrometry. *Nat. methods* **4**, 207–214 (2007).
100. Lapek, J. D. Jr, Lewinski, M. K., Wozniak, J. M., Guatelli, J., Gonzalez, D. J. Quantitative temporal viromics of an inducible HIV-1 model yields insight to global host targets and phospho-dynamics associated with protein Vpr. *Mol. Cell. Proteom.* **16**, 1447–1461 (2017).
101. Wozniak, J. M., Gonzalez, D. J. PTMphinder: an R package for PTM site localization and motif extraction from proteomic datasets. *PeerJ* **7**, e7046 (2019).
102. Xiao, Y. et al. A novel significance score for gene selection and ranking. *Bioinformatics* **30**, 801–807 (2014).
103. Huang da, W., Sherman, B. T., Lempicki, R. A. Systematic and integrative analysis of large gene lists using DAVID bioinformatics resources. *Nat. Protoc.* **4**, 44–57 (2009).
104. Huang, D. W. et al. The DAVID Gene Functional Classification Tool: a novel biological module-centric algorithm to functionally analyze large gene lists. *Genome Biol.* **8**, R183 (2007).
105. Szklarczyk, D. et al. STRING v11: protein-protein association networks with increased coverage, supporting functional discovery in genome-wide experimental datasets. *Nucleic Acids Res.* **47**, D607–d613 (2019).

Acknowledgements

We thank the members of the Newton laboratory and the laboratory of Dr. Jack E. Dixon for helpful discussions and Dr. Roberto Malinow for advice on the electrophysiological approaches. We also thank the Collaborative Center of Multiplexed Proteomics at UCSD for the

phosphoproteomics analysis, Dr. Donald Pizzo from the UC San Diego Human and Animal Tissue Technology Center for processing the histology samples, and Dr. Robert Rissman and Jeffrey Metcalf from the Alzheimer's Disease Research Center (ADRC) Neuropathology Core and Brain Bank at UCSD for providing human brain samples, which were collected with support from the NIH UCSD ADRC Center Grant (NIH AG062429 to RR). The cartoon in Fig. 3a was created with BioRender.com. This work was supported by Cure Alzheimer's Fund (A.C.N. and R.E.T.) and NIH R35 GM122523 (A.C.N.). J.M.W. was supported by the University of California, San Diego Graduate Training Programs in Cellular and Molecular Pharmacology (T32 GM007752) and Rheumatic Diseases Research (T32 AR064194).

Author contributions

G.L., J.M.W., K.D., L.E.D., A.J.R., and C.C.-G. performed the experiments. J.M.W. performed the MS analysis mentored by D.J.G. K.D. performed the electrophysiology experiments. L.E.D. performed the spine density analysis mentored by G.N.P. A.J.R. and C.C.-G. performed the behavioral experiments. R.E.T. coordinated the generation of the mouse models. G.L. and A.C.N. conceived the project, designed the experiments, and wrote the manuscript. All authors edited the manuscript.

Competing interests

The authors declare no competing interests.

Additional information

Supplementary information The online version contains supplementary material available at <https://doi.org/10.1038/s41467-022-34679-7>.

Correspondence and requests for materials should be addressed to Alexandra C. Newton.

Peer review information *Nature Communications* thanks Dario Alessi, Per Nilsson, Jeffrey Savas, and the other, anonymous, reviewer(s) for their contribution to the peer review of this work. Peer reviewer reports are available.

Reprints and permissions information is available at <http://www.nature.com/reprints>

Publisher's note Springer Nature remains neutral with regard to jurisdictional claims in published maps and institutional affiliations.

Open Access This article is licensed under a Creative Commons Attribution 4.0 International License, which permits use, sharing, adaptation, distribution and reproduction in any medium or format, as long as you give appropriate credit to the original author(s) and the source, provide a link to the Creative Commons license, and indicate if changes were made. The images or other third party material in this article are included in the article's Creative Commons license, unless indicated otherwise in a credit line to the material. If material is not included in the article's Creative Commons license and your intended use is not permitted by statutory regulation or exceeds the permitted use, you will need to obtain permission directly from the copyright holder. To view a copy of this license, visit <http://creativecommons.org/licenses/by/4.0/>.

© The Author(s) 2022